Fluid-rock interactions, hydrothermal processes, and accommodation of slip in shallow parts of the San Andreas and San Gabriel Faults, southern California

James P. Evans[1], Kaitlyn A. Crouch[1,2], Caroline Studnicky[1,3], Sharon Bone[4],

Nicholas Edwards[4], Samuel M. Webb[4]

[1]Department of Geosciences, Utah State University, Logan, UT 84322-4505

[2] now at: Department of Geosciences, University of Wisconsin, Lewis G. Weeks Hall, 1215 West Dayton Street, Madison, WI 53706-1692

[3]now at: Chevron North America Exploration and Production, 6301 Deauville Boulevard

Midland, TX 79706, U.S.A.

[4]Stanford Synchrotron Radiation Lightsource, SLAC National Accelerator Laboratory

2575 Sand Hill Road, MS 69 Menlo Park, CA 94025

This is a non-peer reviewed preprint submitted to EarthArXiv. This version of the paper was submitted to Tektonika iin May, 2023.

Abstract

We examine fault-related rocks from the upper parts of the active San Andreas and ancient San Gabriel Faults, southern California, to determine the nature and origin of micro-scale composition and geochemistry of fault-related rocks. These data constrain the nature and extent of fluid-rock interactions and processes by which slip is accommodated on shallow portions of these faults. The steeply dipping San Gabriel Fault (SGF) was sampled in a steeply inclined borehole to a depth of 400 m, and the San Andreas Fault (SAF) was sampled by seven northeast-plunging boreholes to a depth of 250 m. Fault damage zones 100m+ wide exhibit narrow fault core zones within broad damage zones. Petrographic, mineralogic, whole-rock geochemical analyses and synchrotron-based X-ray fluorescence mapping of whole drill core and thin sections reveal evidence for repeated syntectonic hydrothermal alteration, Fe-Mn rich mineralization, shearing, and brecciation that resulted in the formation of foliated cataclasites and clay and chlorite-rich shear zones in fractured network fault zones. Mineralization and alteration include clay and chlorite development, carbonate and zeolite mineralization, and the mobility of trace and transition elements in the deformed rocks. Textural evidence for repeated shearing, alteration, vein formation, brittle deformation fracture, fault slip, pressure solution, and re-lithification of faulted rocks suggests that hydrothermal alteration occurred during deformation at shallow levels. The rock assemblages likely represent significantly weakened rocks that have the potential to slip at low shear stresses, experience creep, distribute seismic energy within and near the fault, and show that hydrothermal conditions in faults may exist at very shallow levels of active faults.

1 INTRODUCTION

Faults in the upper 2 to 5 km of the Earth's continental crust typically do not radiate energy (Scholz, 2019; Xu et al., 2016); yet long-term tectonic slip is accommodated in the shallow zone for crustal strains to be compatible over the entire depth range of a fault (Rice and Tse, 1986; Marone and Scholz, 1988). Seismic energy travels through fault zones to the surface and affects how energy is distributed in and away from the fault. Slip nucleated at seismogenic depths reaches the Earth's surface through an upper aseismic or stably slipping zone (Marone and Saffer, 2007). Coseismic energy is consumed in fault zones by rupture propagation, slip along fault surfaces (Harris and Day, 1997; Andrews, 2005), and by anelastic processes within low elastic moduli fault damage zone rocks (Chester and Logan, 1986; Schulz and Evans, 2000; Roten et al., 2017). The depth distribution of earthquake foci in southern California (Hauksson and Meier, 2019) and inversions of M_b> 7.0 strike-slip faults (Archuleta, 1984; Kaneko and Fialko, 2011; Dolan and Haravitch, 2014; Scott et al., 2019; Xu et al., 2016) show that seismic slip maxima occur at depths of 4 to 10+ km, and slip diminishes to ~ 50% or less of these maxima towards the Earth's surface (Kaneko and Fialko, 2011). Some workers indicate that interpretations of shallow-slip deficits may be due to the assumptions made in modeling fault slip (Marchandon et al., 2021). Resolving modeling uncertainties, establishing the distribution and magnitudes of fault slip as a function of depth, and determining the elastic properties of fault zones over a full depth range are required to resolve the magnitude of shallow slip deficits. The upper portion of faults may experience some combination of coseismic and post-seismic slip or creep after main shocks (Marone and Saffer, 2010) to accumulate the nearly constant amount of slip thought to develop in the brittle layer over long periods (Rice and Tse, 1986).

Mechanisms to explain shallow slip deficits and fault-zone plasticity include frictional slip on weak fault-related rocks, pore-fluid pressure weakening (Marone and Saffer, 2007), or bulk plastic yielding (Roten et al., 2017) due to the presence of lower cohesive and frictional strength rocks in fault damage zones (Chester et al., 1993; Isaacs et al., 2008; Jeppson et al., 2010; Bradbury et al., 2011; Jeppson and Tobin, 2015). Most fault zone classification schemes and interpretations (Sibson, 1977; Woodcock and Mort, 2008) depict the uppermost parts of fault zones as consisting of low or non-cohesive fault zones comprised of 'incohesive breccias'. Most of these models fail to account for the nature and extent of a range of fault-related rocks observed in the rock record, especially foliated fault-related rocks that form in the upper crust (c. f., Chester and Logan, 1986; Chester et al., 1993; Isaacs et al., 2008) and in faults where significant fluid-mediated alteration occurred during deformation (Faulkner et al., 2003; 2010; Smith et al., 2013; Towend et al., 2017; Boulton et al., 2017). Evidence for fault zone alteration, cementation, and mineralization is observed in a range of places along the San Andreas System. Clay ± chlorite ±

phyllosilicate-rich fault-zone rocks are in exhumed faulted rocks (Chester et al., 1993; Moore and Rymer, 2012; Schulz and Evans, 1998; Bradbury et al., 2015) and in the deep SAFOD core (Gratier et al., 2011; Bradbury et al., 2015; Holdsworth et al., 2011; Richard et al., 2014; Schleicher et al., 2009). The presence of such fault-related rocks suggests brittle and non-brittle processes operate at shallow crustal levels in these strike-slip faults, and alteration in fault zones is driven by heat and fluids active in shallow fault regimes. Fluid-rock interactions have been invoked to explain the presence of veins, clay-rich fault gouge, alteration assemblages such as hydrologically driven alteration of hornblende to iron-oxides ± chlorites or feldspars to clay, mineralization within faults, or pressure solution. Some of these processes may occur at ambient thermal conditions, but in many cases, these features likely occurred at hydrothermal conditions—at temperatures above the background geothermal conditions.

These studies beg the questions: 1. What are the structures and composition of the shallowest parts of the bedrock component of faults (Nevitt et al., 2020)? 2. How might these processes lead to coseismic slip deficits (if real) and energy adsorption? 3. What are the processes that are responsible for these deficits, and can we see evidence for them in the rock record? 4. How do indurated fault-related rocks form within the upper few kilometers of the earth's crust? 5. What is the nature and extent of fluid-rock interactions in the shallow parts of fault zones?

We address these questions by examining rocks retrieved from drill core from depths of 100-400 m across an active segment of the San Andreas Fault (Studnicky, 2021; Studnicky et al., submitted; Williams et al., 2021) and from the exhumed San Gabriel Fault (Crouch, 2022; Crouch et al., in revision) at microscopic scales to document the deformation mechanisms, mineralogy, and geochemistry within the damage zones. Narrow slip surfaces in these faults lie within damage zones, where brittle deformation and fluid-induced low-temperature alteration produced regions of intense brittle damage and phyllosilicates ± zeolites ± carbonates assemblages. Samples and borehole-based data from continuously cored boreholes provide samples of the entire fault zones, and the rocks have well-preserved deformation and alteration textures with little surface-related alteration.

We use synchrotron radiation scanning X-ray fluorescence (SRS-XRF) mapping (Bergmann et al., 2018; Edwards et al., 2018) to complement optical and scanning electron microscopy, whole-rock geochemistry, and X-ray diffraction mineralogic analyses of fault-related rocks. Analyses of elemental composition and their variations at mm to 10's cm scales enable us to integrate elemental maps with the results of studies at the drill core and thin section scales to determine how fluid-rock-deformation interactions occurred in the shallow parts of these faults.

1.1 Geologic Setting

We examine two suites of samples across the active San Andreas Fault and the ancient San Gabriel Fault acquired in recent geotechnical drilling studies. The San Andreas Fault (SAF) system accommodates much of the transform plate motion between the Pacific and North American Plates in southern California (Irwin, 1990). In the Mojave region, the active San Andreas Fault [Figure 1] was preceded by slip on the Punchbowl and San Gabriel Faults (SGF) (Powell, 1993; Powell and Weldon, 1992; Nourse, 2002). The Elizabeth Lake study site on the San Andreas Fault (LADWP, 2019; Williams et al., 2021; Studnicky et al., submitted) consists of seven northeast-plunging boreholes drilled to depths of 144 m across the San Andreas Fault [Figure 1; Figure 2a]. These holes were drilled by the Los Angeles Department of Water and Power [LADWP, 2019] where the Los Angeles Aqueduct crosses the fault (Mulholland, 1918; Sutherland et al., 2013). The San Gabriel Fault exhumed in the San Gabriel Mountains [Figure 1C], is exposed at the surface (Anderson et al., 1983; Chester et al., 1993; Evans and Chester, 1995) and is sampled by an ~60°-plunging, 493 m-deep borehole [Figure 2b] that intersects the western San Gabriel Fault shear zones at 313 and 420 m deep (Crouch and Evans, in revision). This hole was drilled for geotechnical investigations by the California High-Speed Rail system and provides a range of data that we use to decipher the elastic and seismic properties of the fault (Crouch and Evans, in revision).

The Mojave segment of the SAF, last ruptured in the 1857 magnitude 7.8 Fort Tejon earthquake (Zielke 2010), and accommodates 22 to 28 mm/yr of slip and an average horizontal displacement of 4 m/event (Scharer and Streig, 2019). The Elizabeth Lake site drilled by the LADWP lies at the transition of the Mojave North and South sections of the fault segment (Field et al., 2014), and is an important site for determining the paleoseismic records of the San Andreas Fault in the region (Bemis et al., 2021). Mesoscopic description of the drill core and geophysical logs of the boreholes [LADWP, 2019], interpretation of the as-built logs of the aqueduct (Sutherland et al., 2014), and analyses of the drill core (Lindvall et al., 2017; Studnicky, 2021; Williams et al., 2021; Studnicky et al., submitted) indicate that the inner part of the fault zone consists of an up to 400 m wide fault zone within a fault (damage?) zone 1 km wide, with several principal slip surfaces that may have experienced ~ 15 cm of slip in the past 100 years (Tayyebi et al. (2017). Rocks northeast of the fault are Late Cretaceous quartz diorite to granodiorite, and the southwestern block is comprised of Cretaceous quartzo-feldspathic and amphibolite gneiss with feldspar, quartz, biotite, and hornblende (Figure 2 b; Dibblee and Minch, 2002; Hernandez, 2011). Regional exhumation is estimated at <2 km (Buscher and Spotila, 2007) in the past 10 My for this area.

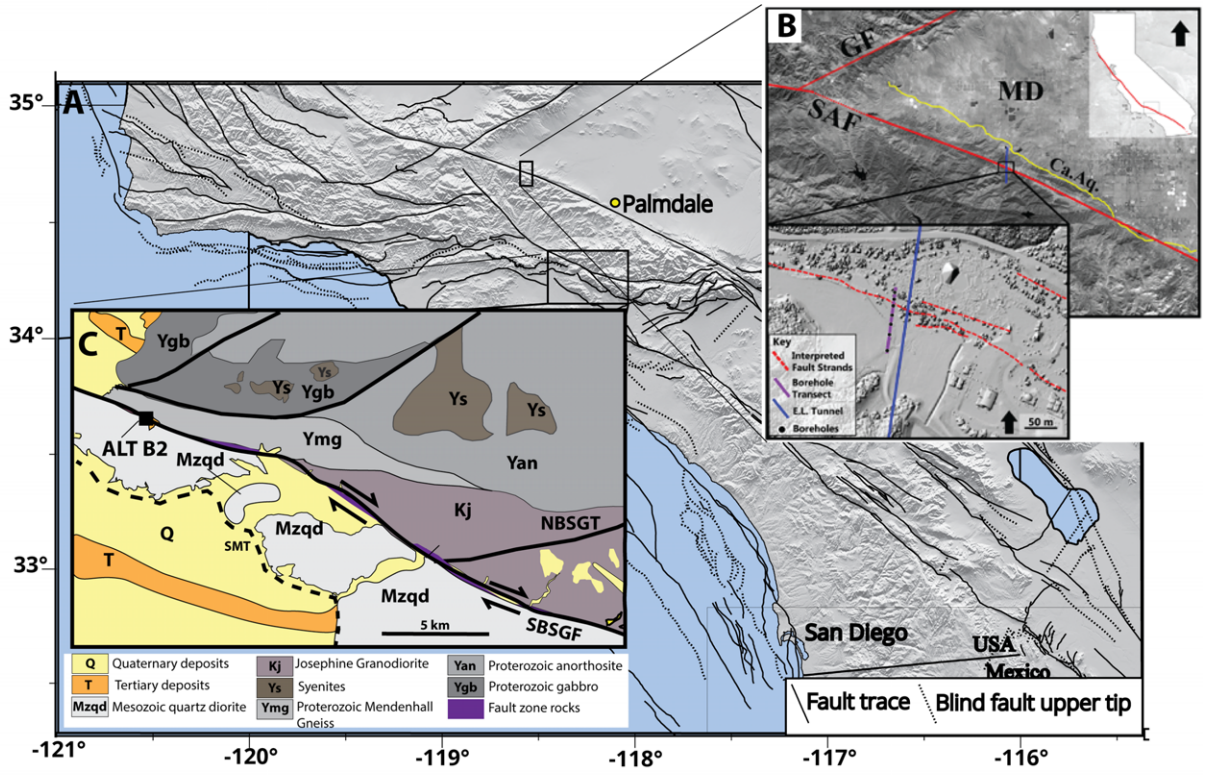

Figure 1. Geologic setting of. the study areas. A) General fault map of southern California with inset maps of the southwestern San Gabriel Mountains, CA, adapted from Yerkes et al., (2005). Blacklines represent active faults from the SCEC CFM5.3 database. B) The Lake Elizabeth site is on the San Andreas Fault. Red lines represent faults. The location map of the Lake Elizabeth transect across the San Andreas Fault zone shows the borehole transect along a 250 m long transect within the ~ 1 km wide valley that forms the topographic expression of the fault. C) Map of the location of California High-Speed Rail Authority ALT-B2 borehole and Little and Big Tujunga field sites along the San Gabriel Fault. Abbreviations: SGF—San Gabriel fault; LT—Little Tujunga; BT—Big Tujunga; Pmgn—Mendenhall Gneiss; Kgrd—Josephine Granodiorite.

Up to 42 km of transform slip was accommodated on the San Gabriel Fault between 13 and 5 Mya (Powell, 1993; Nourse, 2002), and as much as 5 km of post-Miocene slip may have occurred along parts of the San Gabriel and Vasquez Faults (Beyer et al., 2009; Bryant, 2017). The San Gabriel Mountains have been uplifted due to south-directed slip on the underlying north-dipping Sierra Madre thrust fault, and the rocks related to ancient slip on the SGF are exhumed from 2 to 5 km depths (Chester et al., 1993; Spotila, 2002; Blythe et al., 2002) to reveal a narrow fault core along which most of the fault slip occurred within a damage zone (Chester et al., 1993; Evans and Chester, 1995; d'Alessio et al., 2003; Crouch et al., in revision). The drill core extends to depths of 493 m and forms a shallow angle with the steeply dipping San Gabriel Fault [Figure 2b], thereby sampling a large portion of the fault damage zone with little interference from near-surface alteration. Fault-related rocks from the SGF likely formed at 2.5-5.5 km depth, and the protolith consists of the Precambrian Mendenhall Gneiss on the north side of the fault, which consists of migmatitic felsic gneiss and mafic granulite. On the south side, the rocks are mapped as Mesozoic quartz diorite, granite, and tonalite. The modern geothermal gradient in the area is ~25-30°C (Lachenbruch, 1986; Buscher and Spotila, 2007).

2 Methods

Samples for these studies come from drill cores acquired across the fault zones (Figure 2; Studnicky et al., submitted Crouch and Evans, in revision). Core-based studies of fault zones provide less altered rocks that have better-preserved alteration and deformation textures (Boulton et al., 2017; Bradbury et al., 2011; Duan et al., 2016). The mesoscopic analyses of the drill core, microstructural analyses of deformed rocks, and mineralogy from X-ray diffraction studies for these boreholes (Studnicky et al., in preparation; Williams et al., 2021; and Crouch and Evans, in revision) guide the analyses of the microchemistry with synchrotron radiation scanning X-ray fluorescence (SRS-XRF) at the Stanford Synchrotron Radiation Laboratory (SSRL). Twenty-two samples with 52 elemental map regions from the San Gabriel Fault and 17 samples with 48 from the Lake Elizabeth site were examined. The incident beam energy, spot size, and dwell times are consistent for all of the analyses. The SRS-XRF enables rapid elemental concentration analyses across the same map areas as viewed in thin sections. For details of the analytical methods and settings for the micro-XRF mapping, see Appendix 1. We focus on the whole-rock geochemistry and microchemistry revealed at the grain and mm-scales, and the implications of the alteration and mineralization for the shallow behavior of active fault zones. Details of how the drill core was acquired are described in Crouch and Evans, in revision, and Studnicky (2021).

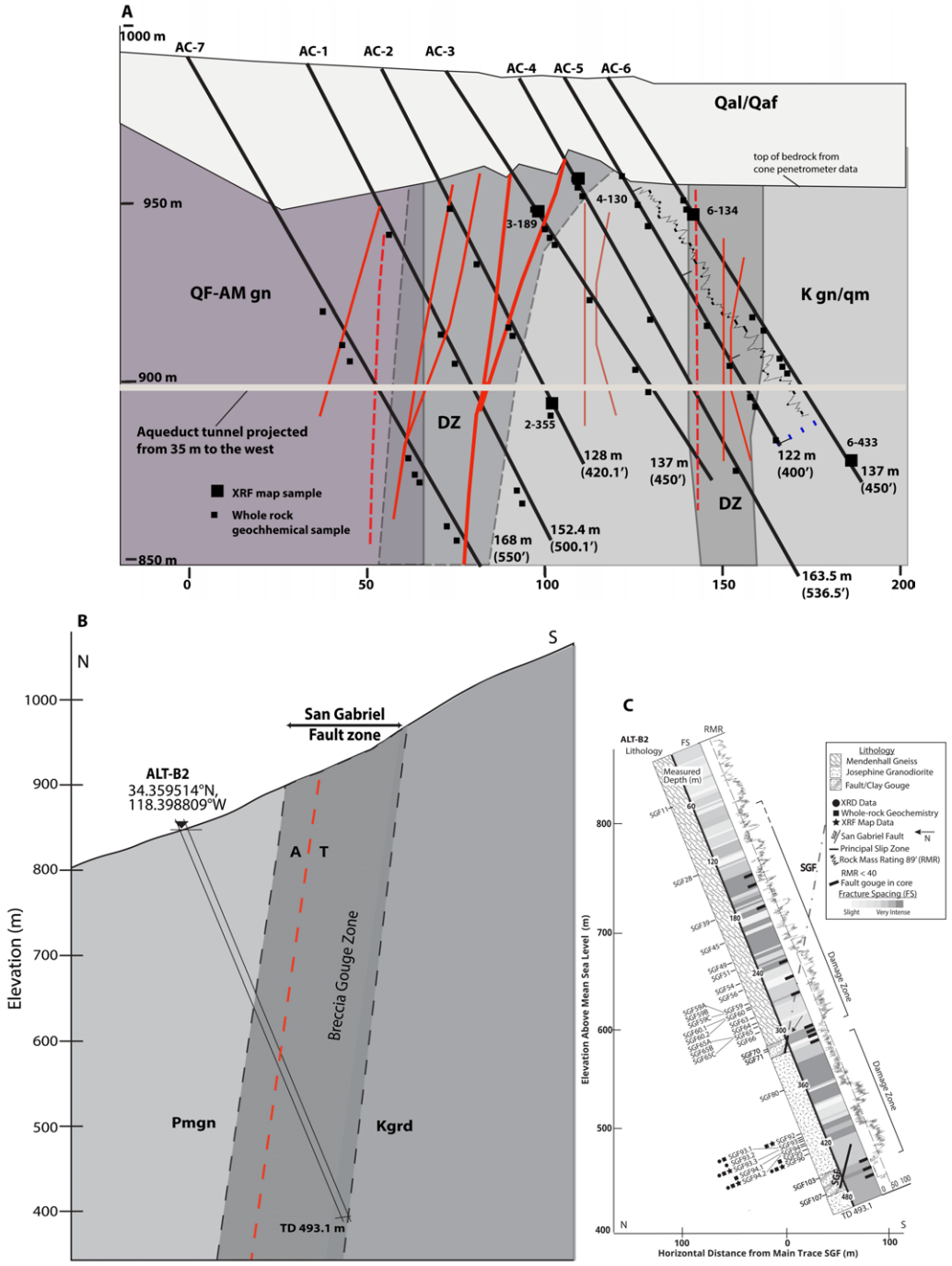

Figure 2. Cross sections of study areas. A) Cross section of inferred fault structure and associated damage zones of the San Andreas fault, with the locations of the boreholes. Modified from the LADWP Final Report (LADWP, 2019) and Studnicky et al., submitted. The simplified geology of the drill site shows damage zones (DZ), interpreted from core logs and resistivity logs, which are 20-60 m thick and contain narrow slip surfaces defined by the presence of cataclasite and ultracataclasite in the core. Rocks southwest of the fault zone (Pacific side) consist of quartzo-feldspathic and amphibolite gneiss (QF-Am gn). Rocks to the northeast, on the North American side, are Cretaceous granodiorite-to-quartz monzonites (K Gn-qm). Shallow auger boreholes and cone penetrometer tests in the Quaternary sediments indicate the

presence of two 5-7 m high steps in the contact between the bedrock and the Quaternary deposits (Qal and Qaf), are interpreted to be aligned with the active trace of the fault from the work of Scharer et al. (2019) and Bemis et al (2021). A simplified short resistivity log is shown for borehole AC-5.

B) simplified borehole ALT-B2 cross-section adapted from CHSRA drill logs (CHSRA, 2019; Crouch and Evans, in review). The ALT-B2 borehole plunges 68° south through the SGF to a total depth of 493.1 m. Simplified lithology, fracture density, locations of core samples, geochemical data, and the locations of the fault zone from Crouch et al., submitted, and Crouch, 2022. Lithology consists of Mendenhall Gneiss to 313 m depth and Josephine Granodiorite to the bottom. ALT-B2 shows two principal slip zones, two damage zones, two highly fractured zones, and two zones of lower fracture intensity and plastic shear (blue arrows). Kelly Bushing height is 864 m MSL. C) Detailed log of the ALT B2 borehole, with sample locations, and rock mass rating (RMR) from geotechnical reports, with low-value zones (<40) RMR values (based on Crouch and Evans, submitted) that indicate the presence of low-strength rocks. The rock mass rating is a measure of macroscopically determined rock strength, based on fracture spacing, core recovery, and experimentally determined strengths. The fracture spacing is at least one fracture every: slight=30-90 cm; moderate=10-30 cm; intense= 2.5-10 cm; very intense= <2.5 cm.

Whole-rock geochemistry major-, minor-, trace-, and rare-earth element analyses were performed on 46 samples from the Lake Elizabeth samples and 41 drill core samples and 9 outcrop samples from the San Gabriel Fault by ALS Geochemistry Labs using X-ray fluorescence, Inductively Coupled Plasma Atomic Emission Spectroscopy (ICP-AES), and Inductively Coupled Plasma Mass Spectrometry (ICP-MS) analyses on ~ 2 g aliquots. For the San Gabriel Fault site, we compare our data with the whole-rock geochemistry data of Anderson et al. (1983), Barth et al. (1995 a, b), and Evans and Chester (1995). For the Lake Elizabeth site, we used whole-rock data from quarto-feldspathic protolith geochemical analyses from studies on nearby rocks north of the site (Ross, 1984; Weschler et al., 2011) to compare our protolith values.

We used bootstrapping statistical analysis (Bendat and Piersol, 2000; Sohn and Menke, 2002) on the whole-rock XRF data with 90% confidence intervals and 1500 iterations (see Williams et al., 2021) to estimate possible groupings of the rock types and their variations within the fault zone. Bootstrapping enables us to estimate standard errors and confidence intervals of the closed whole-rock major-element data and does not rely on *a priori* assumptions for the data distribution. We adopted a bootstrap script provided by R. Williams (written comm., 2021) as modified in Studnicky (2021) and Crouch (2022).

In related studies (Crouch and Evans, in revision; Studnicky et al., in prep.), we examine the deformation microstructures and textures with optical and secondary and back-scattered electron microscopy to constrain mesoscopic deformation textures and inferred processes from the shallow parts of the faults. Here we apply SRS-XRF to examine major-, minor-, and trace-element distributions in deformed rocks from the brittle and semi-brittle deformed fault zones. Synchrotron-based analyses (Brown et al., 1998; Kelly et al., 2008; Renard et al., 2016; Bergmann et al., 2019) have been used to examine a range of geologic, archeologic, palaeontologic, and art materials, but have seen relatively little use in the low- to moderate T-P deformation realm (Fusseis et al., 2014). We adapt techniques developed by these workers, along with new developments (Edwards et al., 2018), to examine altered and deformed fault-related rocks from active and ancient strands of the San Andreas Fault zone in southern California. X-ray fluorescence mapping is well-suited for high-resolution spatial analyses of elements in deformed rocks that have several advantages relative to other methods. Little to no sample preparation or polishing is needed. Small, rare, and delicate samples or samples with fine-scale fabrics can be examined with little or no loss of sample. Samples stabilized in epoxies can also be examined with no analytical interference from fixing compounds. The analyses are done at ambient temperatures and pressures, so there are no issues with vacuum and degassing from samples with volatile content.

The sample holders, beamline configurations, and data acquisition software at SSRL enable us to characterize standard 2 x 3 cm and 5 x 7.5 cm thin sections as well as 60-80 cm long pieces of core. We

use low-resolution rapid scans to determine the general character of the elemental distributions and very high-resolution analyses in similar beam conditions. This enables us to analyze s 10^{-6} to 10^{-1} m-scales with the same analytical conditions. Data for up to 16 elements are collected for rapid data interrogation at the beamline, and the full XRF spectrum per pixel data set is also collected concurrently for more time-consuming post-experiment in-depth interrogation of the data.

Geochemical and mineralogic analyses of rocks from shear zones (e.g., Mitra, 1978; Simpson, 1985) and semi-brittle to brittle fault zones (Mitra et al., 1984; Evans and Chester, 1995; Boulton et al., 2017) define physio-chemical processes and evolution of ductile shear and brittle fault zones. Chemical and mineralogic characterizations of deformed rocks are fundamental to determining the composition of these rocks, which then informs models of rock properties and their changes over the history of the sheared rocks (Niemeijer et al., 2016; Faulkner et al., 2010; Mitchell and Faulkner, 2009). Variations in major-, minor-, and in many cases, trace-element distribution and concentrations provide valuable insights into the nature and degree of fluid-rock / hydrothermal processes in faults and determine the mineral composition and distribution that influence the mechanical behavior and textures of these sheared rocks. X-ray diffraction studies to determine mineralogic characteristics of the fault-related rocks are presented in Crouch et al., in review, and Studnicky et al., submitted.

2.1 Distribution of metals

We examine metals between Na and Zn, with particular focus on Ca, Ti, V, Cr, Mn, Fe, Ni, and in some cases, Zn and S. These elements exhibit variations associated with textures of faulted and altered rocks of the San Andreas and San Gabriel faults (Bradbury et al., 2015; Evans and Chester, 1995). These elements have a range of reduction potentials and solubilities in fluids, resulting in diverse geochemical behaviors depending on the nature of fluids, pO_2 values, and other factors. They are among the most abundant minor- and trace elements in the upper crust, and transition metals can form a range of oxides and sulfides in hydrothermal and altered rocks. Iron, manganese, and other metals are often concentrated in faults and shear zones (Evans and Chester, 1995; O'Hara, 1988) and are used to examine the nature of fluid-rock interactions in deformed rocks

Many of the rocks we study consist of dark to optically opaque mm- to cm-thick brown and black material (e.g., Chester et al., 1993). These zones are typically enriched in Fe, Mg, and Mn, likely the result of the alteration of Fe-bearing minerals from fluid-rock interactions (Evans and Chester, 1995). At upper crustal conditions, Ti through Ni are broadly lithophile and siderophile, and analyses of these elements help determine the origin and texture of these fine-grained fault-related rocks. Concentrations and

distributions of these elements vary across sheared rocks, and these elements can occur in a range of oxidation states, thus helping constrain the pH, temperature, anion composition (oxide vs. sulfides), and the nature of fluid-rock /hydrothermal or solution processes in these rocks. These elements exhibit a significant range of concentrations (10-100x) over the concentrations in undeformed granitoid rocks, providing robust analytical chemical signatures.

Since we examined samples in the energy range optimized for first-row transition metals, general comparisons among Fe, Ti, Mn, Cr, and Ni are valid. It is not warranted to compare the low counts of lighter elements (e.g., Ca, K) with Fe, but it is valid to note variations of the values of a given element within a map.

3 Results

3.1 Mesoscopic Fault Structure

The inner, most highly deformed portion of the San Andreas Fault zone at Elizabeth Lake is a ~ 300-400 m wide damage zone as determined from core logging (Figure 2a; Studnicky, 2021; LADWP, 2019), wireline log data from the LADWP project and the as-built data for the aqueduct (Mulholland, 1918; Sutherland et al., 2013), and fault-rock analyses (Wiliams et al., 2021; Studnicky, 2021). The likely main fault zone dips steeply south [Figure 2a] and is expressed as several 5-10 cm thick zones of ultracataclasites within fractured, faulted, and chloritically altered clay-rich slip zones within the damage zone rocks [Figure 2b]. At the top of the bedrock, cone penetrometer data indicate the location of two fault strands (Figure 2a) that offset the contact between the bedrock and unconsolidated sediment. These active traces are extrapolated downdip into the core and are expressed as zones of dark brown, green, and black cataclasites in highly deformed and altered rocks (Wiliams et al., 2021; Studnicky, 2021). Highly deformed clay-rich faults (Williams et al., 2021) are interspersed with less deformed cataclasites and damage zone rocks, but all rocks in the drill core exhibit some level of damage (Studnicky et al., submitted). These zones consist of chlorite ± calcite ± epidote ± clay shear zones, cataclasites, and regions of altered rocks that include calcite, zeolites, chlorite, and Fe-oxides. Sharp boundaries define fault slip zones, and clasts of earlier-formed cataclasite are present (Figure 3).

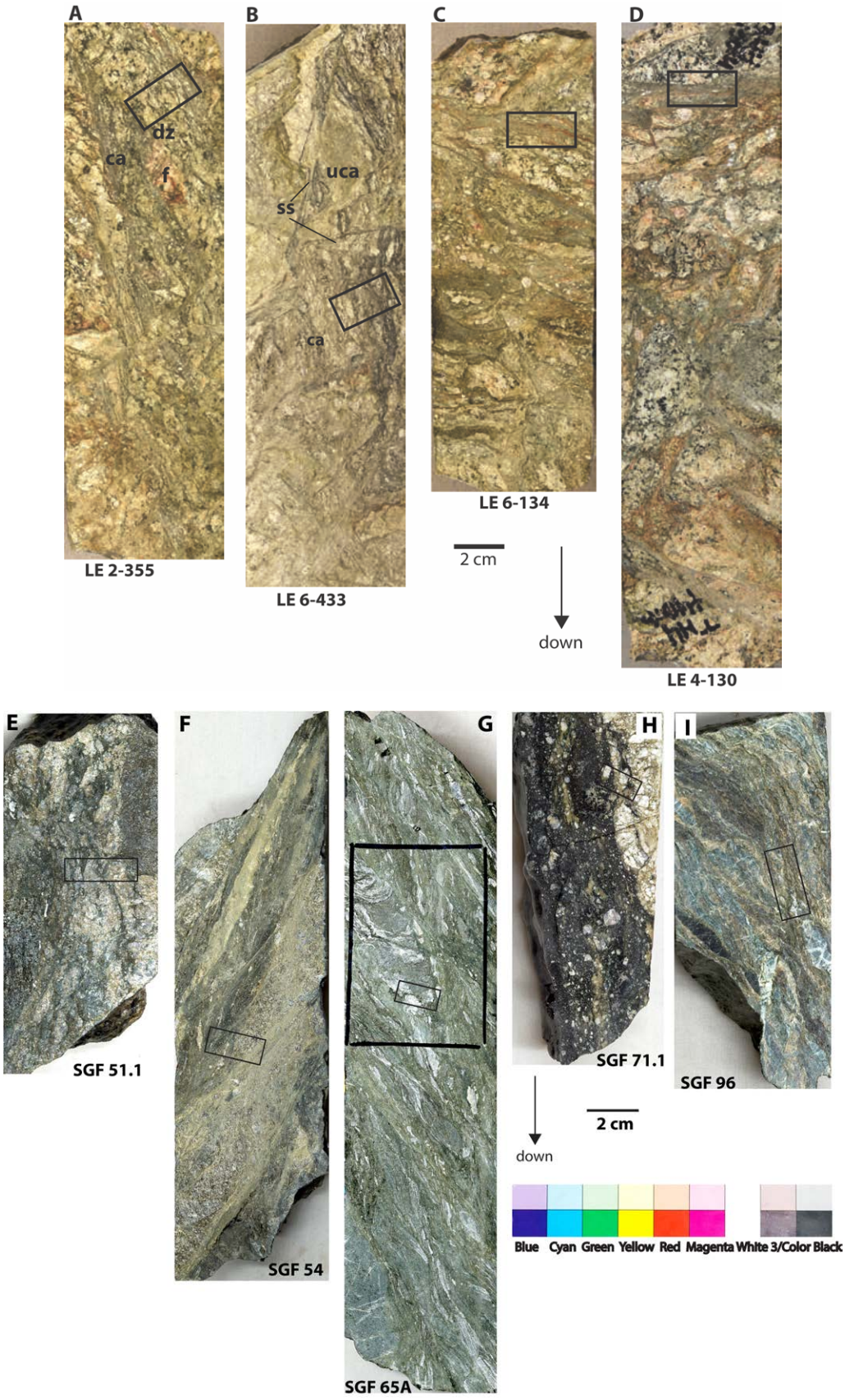
A
dż
ca
f
LE 2-355
B
uca
ss
ca
LE 6-433
C
LE 6-134
2 cm
down
D
LE 4-130
E
SGF 51.1
F
SGF 54
G
SGF 65A
H
SGF 71.1
I
SGF 96
2 cm
down
Blue Cyan Green Yellow Red Magenta White 3/Color Black

Figure 3. Photographs of the core from the Lake Elizabeth core across the San Andreas and the ALT B2 core across the San Gabriel Faults were examined with XRF mapping. Boxes indicate the locations of the. XRF map samples. A) Sample LE 2-355. A sheared rock consisting of brittly deformed damage zone rocks (dz), thin cataclasite (ca), and feldspars (f). B) Sample 6-133. Ultracataclasite (uca) and cataclasite (ca) are cut by narrow slip surfaces (ss). C) Sample LE 6-134. Narrow slip surfaces with concentrations of iron marked by the red regions. D) Sample LE 4-130. Damage with narrow slip surface near the top. E) Sample SGF51.1. Damaged rocks in the protolith F). Damage zone sample SGF 54 with chloritic+ epidote-rich shear zones. G) Sample SGF 65A of highly sheared chlorite+ carbonate + zeolite in the fault core. H) Sample 71.1 of light-colored brecciated quartzo-feldspathic rocks and dark catataclasites. I) Sample SGF 96 of highly sheared rock with thin slip surfaces.

In field exposures, the San Gabriel Fault is 1-10 cm wide (Anderson et al., 1983; d'Alessio et al., 2003; Chester et al., 1993; Evans and Chester, 1995; Crouch and Evans, in revision) within adjacent intensely deformed zones 5-10 m wide, and a ~ 100 m thick damage zone. At depth in the borehole, the fault core is as much as 1-3 m thick within a damage zone ~ 170 m wide. Indurated medium foliated gneiss gives way to chlorite-deformed feldspar altered host rock and shear zones [Figure 2b], and rocks near the central fault zone are chloritic breccia, cataclasites, and foliated cataclasites (Figure 2d; Figure 4; Crouch, 2022; Crouch and Evans, in revision). Rocks from the San Gabriel Fault (Figure 3) range from protolith and sheared chloritic breccia (Figure 3a), and thin ultracataclasite and cataclasite (Figure 3b). Rocks in the southwestern damage zone consist of foliated shear rocks with calcite veins and zeolite layers (Figure 3c) and highly sheared, extremely fine-grained foliated cataclasites and phyllonites (Figure 3 d,e).

A wide range of microstructures developed in the San Andreas Fault, including fractures, small faults, cataclastic zones in the slightly and moderately deformed rocks [Studnicky, 2021; Studnicky et al., submitted], and clay-rich foliated cataclasite which contain clasts of cataclasite within them. We examined an ~60 cm long section of drill core from a portion of the SAF damage zone rocks with rock-core scale XRF mapping analyses (Figure 4). This sample is from the damage zone of one of the inferred active traces of the San Andreas Fault (Figure 2) at a drill core depth of 58 m and a true vertical depth of ~ 36 m, downdip

of the inferred offset of the base of the Quaternary deposits. The sample consists of several narrow dark

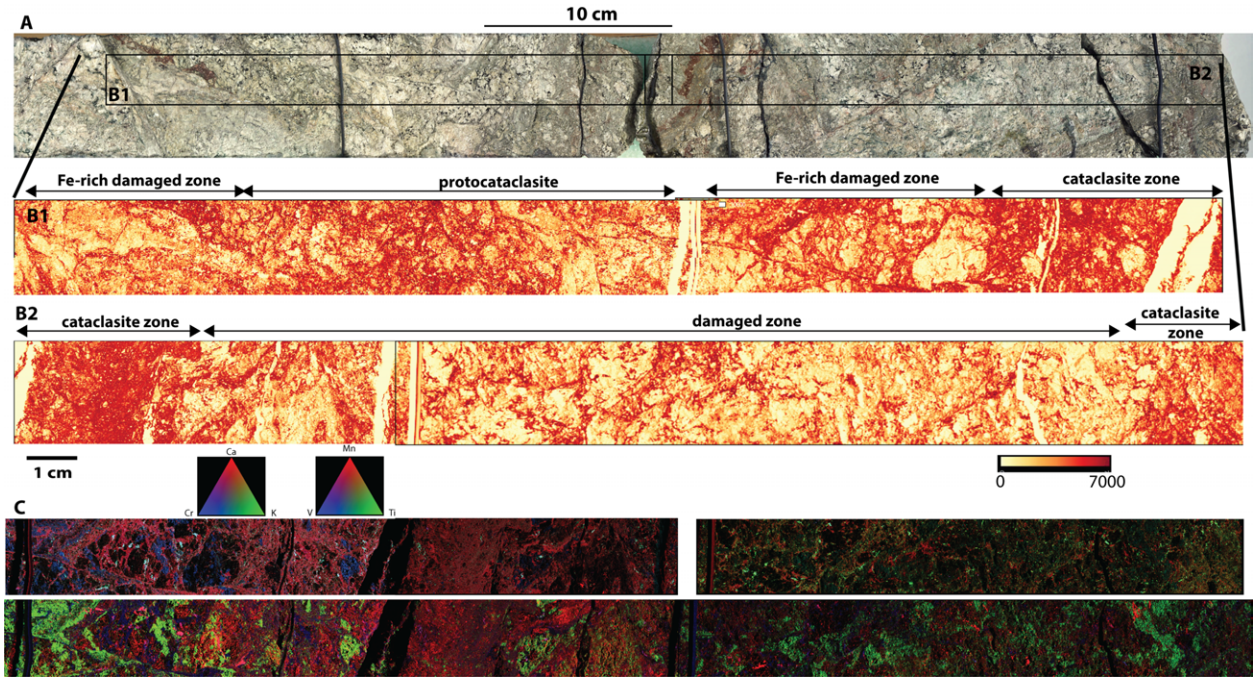

Figure 4. Macroscopic X-ray fluorescence maps of a portion of the core from the damaged zone rocks of the San Andreas Fault. A) Optical image of the entire core section with the zone examined in the X-ray map outlined in the rectangular box. The sample is from the damage zone sampled in core sample 3-189, 60 cm long and 5 cm diameter, examined in beamline 6-2 at SSRL (see Edwards et al., 2018). The chalky white to pink regions are feldspars, most of which exhibit core-scale alteration textures, and several green-gray cataclasite zones. B). Map of iron in the analyzed section. The scale is counts/second. The distribution of iron shows that narrow zones, network of Fe-rich zones in the damaged zone weave throughout the rock, and as highly enriched cataclasite zones consist of fine-grained, amorphous Fe-rich zones. C) Tricolor maps of the distribution of Mn, Ti, and V in the damage zone rocks, and D) Tricolor maps of the distribution of Ca, Cr, and K in the core. The uphole portion of the core (left) In rich in Mn, and the down-hole portions are less so. The uphole region contains irregular zones of V and K, with small regions of Cr concentrations. The downhole region also contains small regions of Ti, denoting the presence of titanite (?). Calcium is ubiquitous in the core.

green-dark grey-red fault zones 1 -5 cm thick surrounded by chalky white to red fractured rocks (Figure 4A) and indurated narrow red and green zones of concentrated slip. Compositional variations are marked by the distribution of iron (Figure 4b), where damage zone rocks consist of Fe-coated fractures, mm- to cm-thick Fe-rich cataclastic zones, and Fe distributed throughout the damage zone matrix. In places, the networks consist of fractures with relatively straight fractures, whereas the bulk of the damage zone imaged reveals irregular Fe-rich zones. Iron-rich damage zones have higher Fe concentrations, and the fracture zones are characterized by thicker through-going Fe-rich zones with mm- to cm-scale protolith clasts. Cataclasite zones are 5 – 10 cm thick and have up to 6 wt. % Fe and Ca are concentrated along planar fractures, likely along feldspar cleavage fractures. In some places, these fractures appear to coalesce and form through-going zones. Transition elements Cr, Mn, Ti, and V, and major elements Ca and K (Figures 4 C, D; Supplemental Figure 1), reflect subtle variations that may mark fluid pathways. Manganese closely correlates with Fe (Supplemental Figure 1) and V lies in irregular zones (Figure 4C) typically associated with K (Figure 4D), and with Ti in small elongate regions. Downhole, Ti is common as small equant zones, perhaps reflecting the presence of titanite. Irregular K-rich regions uphole are associated with chalky white zones, and Cr is distributed through the sample in small irregular zones (Figure 4D). Small Ca-rich veins (Figure 4D) cutting the host rock consist of fractured potassic feldspar zones.

Samples from the San Gabriel Fault include similar structures, and both faults may also provide evidence for the presence of pseudotachylyte [Crouch, 2022; Crouch and Evans, in revision]. Optical petrography and X-Ray diffraction analyses show that the protolith gneiss is moderately to highly altered within the fault damage zones. In the San Andreas Fault, the common alteration assemblages are calcite, zeolites (primarily laumontite, wairakite, and heulandite), chlorite, smectite, hematite, and epidote. In the San Gabriel Fault, the host rock consists of quartz, albite, anorthite, and muscovite. In the damage zone, smectite, phlogopite, calcite, and undifferentiated zeolites are present. In the highly sheared rocks, Ti and Mn oxides, epidote, and clinochlore appear throughout the damage zone. These minerals are sheared, occupy fractures, and appear to replace feldspars, amphiboles, or biotite.

3.2 Geochemical Analyses of Fault-Related Rocks

Whole-rock geochemical analyses for rocks from both fault zones show that the damaged zone rocks are moderately to significantly deformed and altered, with the presence of clays, calcite, zeolites, iron oxides, and chloritic minerals (Crouch and Evans, in revision; Studnicky et al., submitted,. Williams et al., 2021). The whole-rock major-, minor-, and trace-element geochemical analyses of samples from the Lake

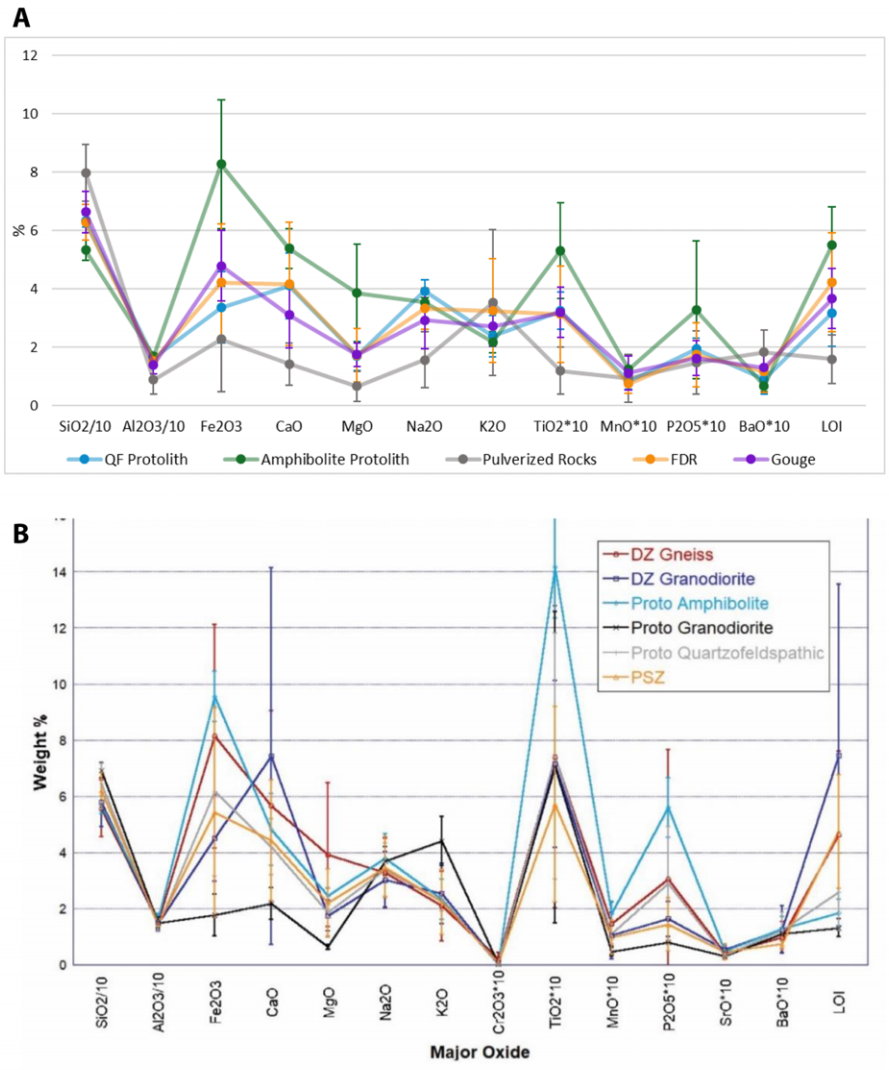

Figure 5. Plots of the whole-rock, major element analyses of samples from the two fault zones. The values of the main rock types are shown, as the means from the different rock types. A) Results from the Lake Elizabeth site**,** with calculated standard deviations for the five rock types identified in the core. Comparison of quartzo-feldspathic protoliths from surrounding areas and Elizabeth Lake XRF data. Samples from this study include quartzo-feldspathic protolith that includes data from Fairmont Reservoir and the Littlerock Creek sites, north of the fault zone from (Ross, 1984) and Littlerock Creek (Weschler et al., 2011) are used to define the QF protolith on the North American side of the fault. EL QF – Elizabeth Lake quartzo-feldspathic protolith. B) Results from the San Gabriel Fault. Average major element compositions of rock types, with calculated standard deviations. The LOI values are 2-5% higher in damaged and altered rock than in protolith. The granodiorite damage zone shows 5% higher Ca values than protolith and the gneissic damage zone shows <2% higher Ca values.

Elizabeth site are augmented with analyses of protolith to the north by Ross (1984) and to the south by Weschler et al. (2011) to provide us with analyses of protolith samples away from the highly deformed rocks (Figure 5; Table 1). Based on core descriptions, optical petrography and mineralogical analyses Five rock types in the San Andreas Fault (Figure 5a) are quartzo-feldspathic (QF) protolith, amphibolite protolith, pulverized rocks, fault-damaged rocks, and gouge (Figure 5a; Studnicky et al., submitted; Studnicky, 2021). The fault-damaged rocks and the gouge are similar to the quartzo-feldspathic protolith. There is a slightly higher abundance of iron-oxides within the fault-damaged rocks and gouge samples than in the quartzo-feldspathic protolith (Figure 5). Studnicky (2021) also documents the presence of SiO_2-rich pulverized rocks that are the result of fragmentation and cementation within the fault zone. These pulverized samples consist of intensely comminuted fault-related rocks that are found in the Lake Elizabeth drill core as small regions of highly lithified, nearly pure quartz cataclasite (Studnicky, 2021).

Fault-related damage zone exhibits a range of values of loss on ignition (LOI) constituents, typically H_2O ± CO_2, from <1 wt% to > 8%; damaged zone rocks have similar values for the other major elements (Figure 6). Relative to these additions, the damage zone and highly sheared rocks from the principal slip surfaces are relatively depleted in Si, K, and Na (Figure 5). The damaged zone and fault gouge rocks are slightly enriched in Fe and LOI relative to the granodiorite protolith and slightly depleted in Na and Ca relative to both protoliths (Figure 5).

We identified six rock types in the San Gabriel Fault zone (Figure 5b: Crouch, 2022; Crouch and Evans, in revision) defined by mesoscopic and microscopic characteristics. These are the Mendenhall Gneiss protolith (separated into amphibolite and quartzo-feldspathic protoliths), Josephine Granodiorite protolith, gneissic damage zone north of the SGF from 120-313 mmd in the borehole, granodiorite damage zone south of the SGF from 325-465.5 mmd, and the principal slip zone rocks. Whole-rock geochemical data (Table 2; Figure 5) show that the granodiorite protolith shows relatively low Fe, Mg, and Ca values, and high K content (Figures 5, 7). The amphibolite protolith is rich in Fe, Ti, and P. The granodiorite and quartzo-feldspathic protoliths have the highest Si content and the amphibolite and damage zones have the lowest Si content. Concentrations of Fe, Ca, Mg, and P values are highly variable across the rock types. The altered and damaged rock exhibit 2-5% higher values of loss on ignition (LOI) than protolith. The LOI value is a proxy for the volume of fluids and other volatiles in deformed rocks and is, therefore, a method of assessing the fluid-rock interaction in the fault zone (Evans and Chester, 1995). The damage zones show relatively high Ca values, with the granodiorite damage zone showing 5% higher Ca values than the granodiorite protolith and the gneissic damage zone showing <2% higher values of Ca than the amphibolite and quartzo-feldspathic protoliths (Figure 5b).

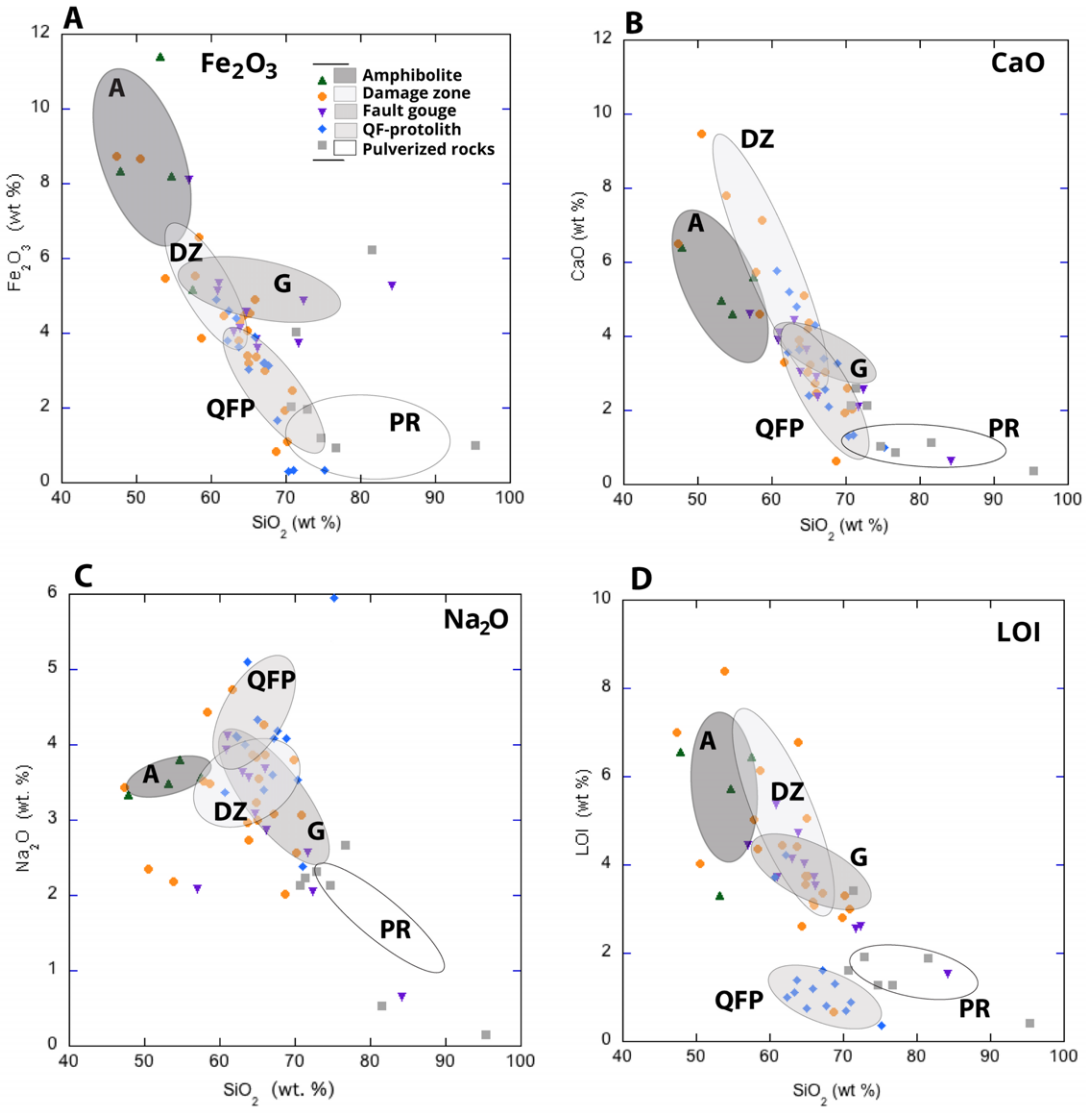

Figure 6. Scatter plots of the whole-rock geochemical analyses for Fe, Ca, Na, and loss-on-ignition values and the results of bootstrap analysis for the Lake Elizabeth site. The ellipses are the 90% confidence uncertainty ellipses that identify likely elemental groups based on the bootstrap analyses for samples from the San Andreas Fault samples. Major oxides are plotted against SiO_2. The rock types determined from the microscopic nature of textures and mineralogy and X-ray diffraction analyses are also differentiated by the whole-rock chemistry. A) Total Fe, reported as Fe_2O_3, as a function of SiO_2. B) CaO as a function of SiO_2. C) Na as a function of SiO_2. D) Loss on ignition as a function of SiO_2. The error ellipses show that the fault damage rocks (FDR) and gouge exhibit Fe, Na, and LOI values that are intermediate between the amphibolite and quartzo-feldspathic protoliths. The Ca values indicate that calcium in the damage zones rocks are enriched relative to the other rock types.

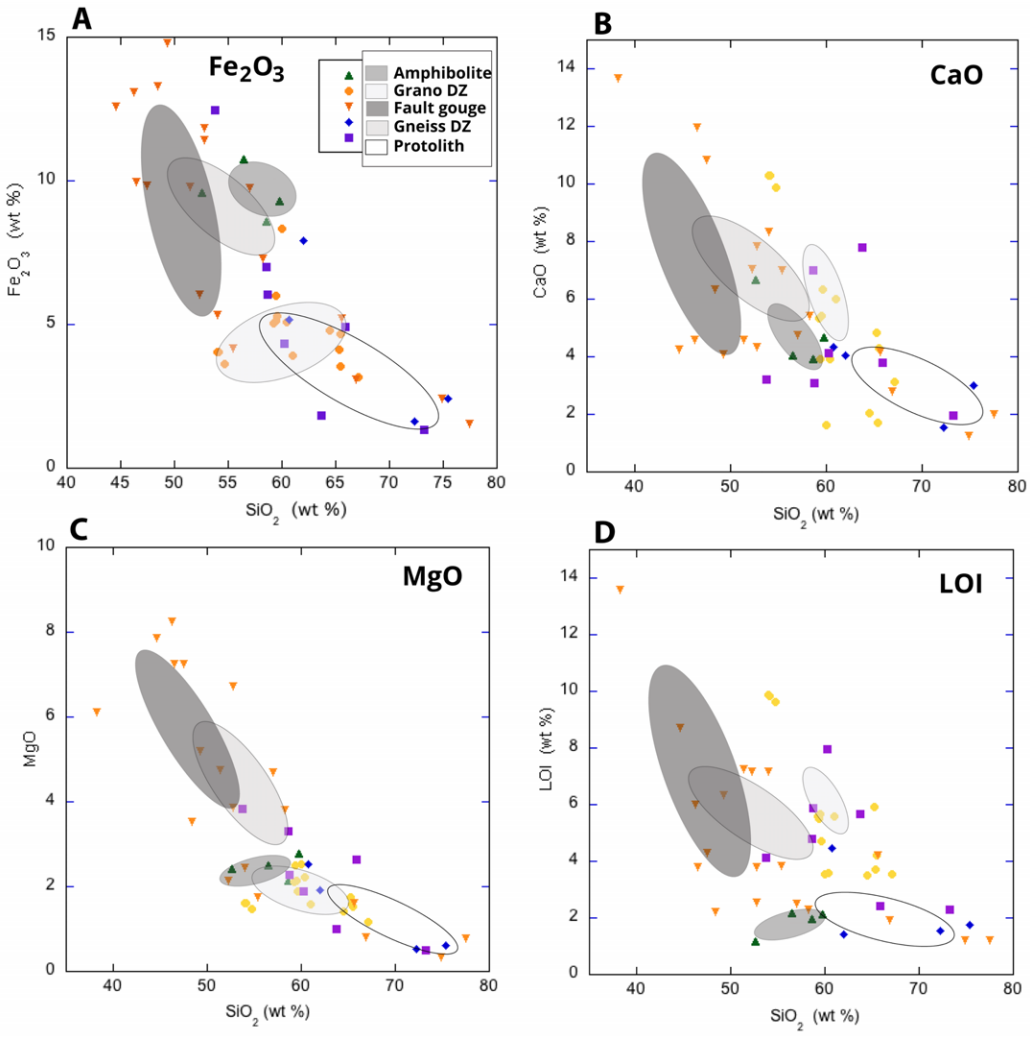

Figure 7. Scatter plots of the whole-rock geochemical analyses for Fe, Ca, Mg, and loss-on-ignition (LOI) values and the results of bootstrap analysis for the San Gabriel fault site. The ellipses are the 90% confidence uncertainty ellipses form likely elemtna groups from bootstrap analyses for samples from the samples. Major oxides are plotted against SiO_2. The rock types determined from the microscopic nature of textures and mineralogy and X-ray diffraction analyses are also differentiated by the whole-rock chemistry. A) Total Fe, reported as Fe_2O_3, as a function of SiO_2. B) CaO as a function of SiO_2. C) Mg as a function of SiO_2. D) Loss on ignition as a function of SiO_2. The error ellipses show that the fault gouge values are enriched in Fe, Ca, Mg, and LOI relative to protolith and damage zone rocks. Damage zone rocks have values of Fe and LOI values are intermediate between the protolith values.

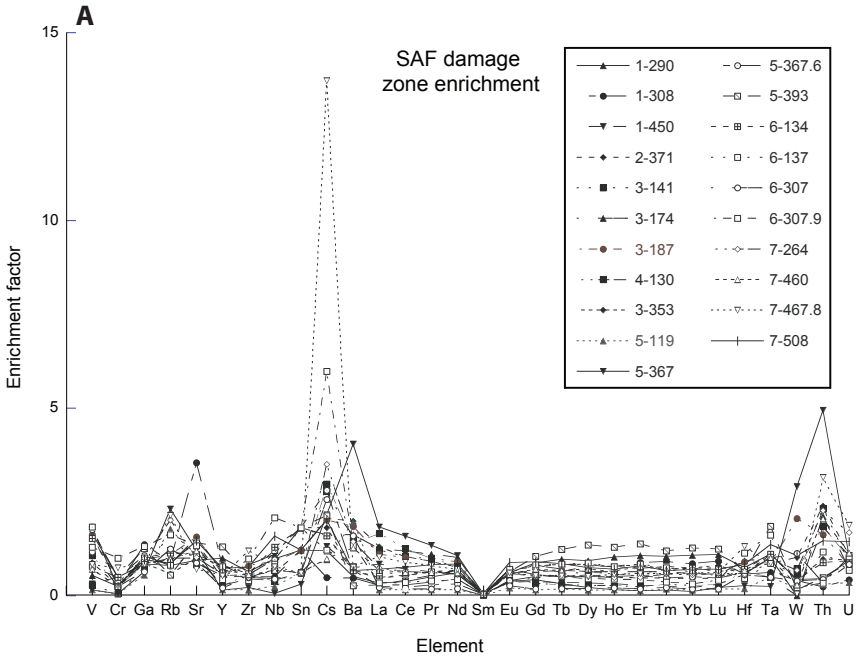
A
SAF damage
zone enrichment
1-290
1-308
1-450
2-371
3-141
3-174
3-187
4-130
3-353
5-119
5-367
5-367.6
5-393
6-134
6-137
6-307
6-307.9
7-264
7-460
7-467.8
7-508
Enrichment factor
Element
V Cr Ga Rb Sr Y Zr Nb Sn Cs Ba La Ce Pr Nd Sm Eu Gd Tb Dy Ho Er Tm Yb Lu Hf Ta W Th U

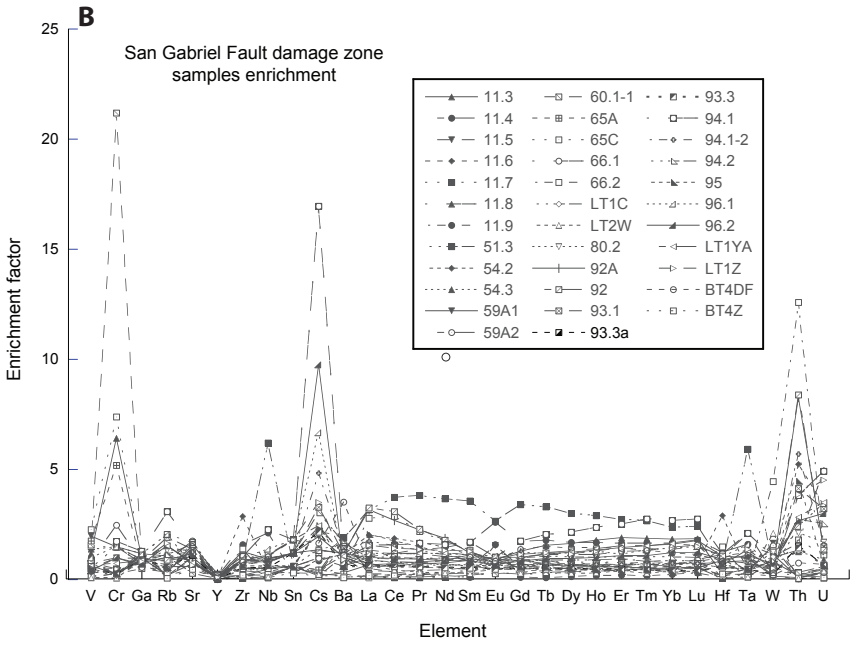
B
San Gabriel Fault damage zone
samples enrichment
11.3
11.4
11.5
11.6
11.7
11.8
11.9
51.3
54.2
54.3
59A1
59A2
60.1-1
65A
65C
66.1
66.2
LT1C
LT2W
80.2
92A
92
93.1
93.3a
93.3
94.1
94.1-2
94.2
95
96.1
96.2
LT1YA
LT1Z
BT4DF
BT4Z
Enrichment factor
Element
V Cr Ga Rb Sr Y Zr Nb Sn Cs Ba La Ce Pr Nd Sm Eu Gd Tb Dy Ho Er Tm Yb Lu Hf Ta W Th U

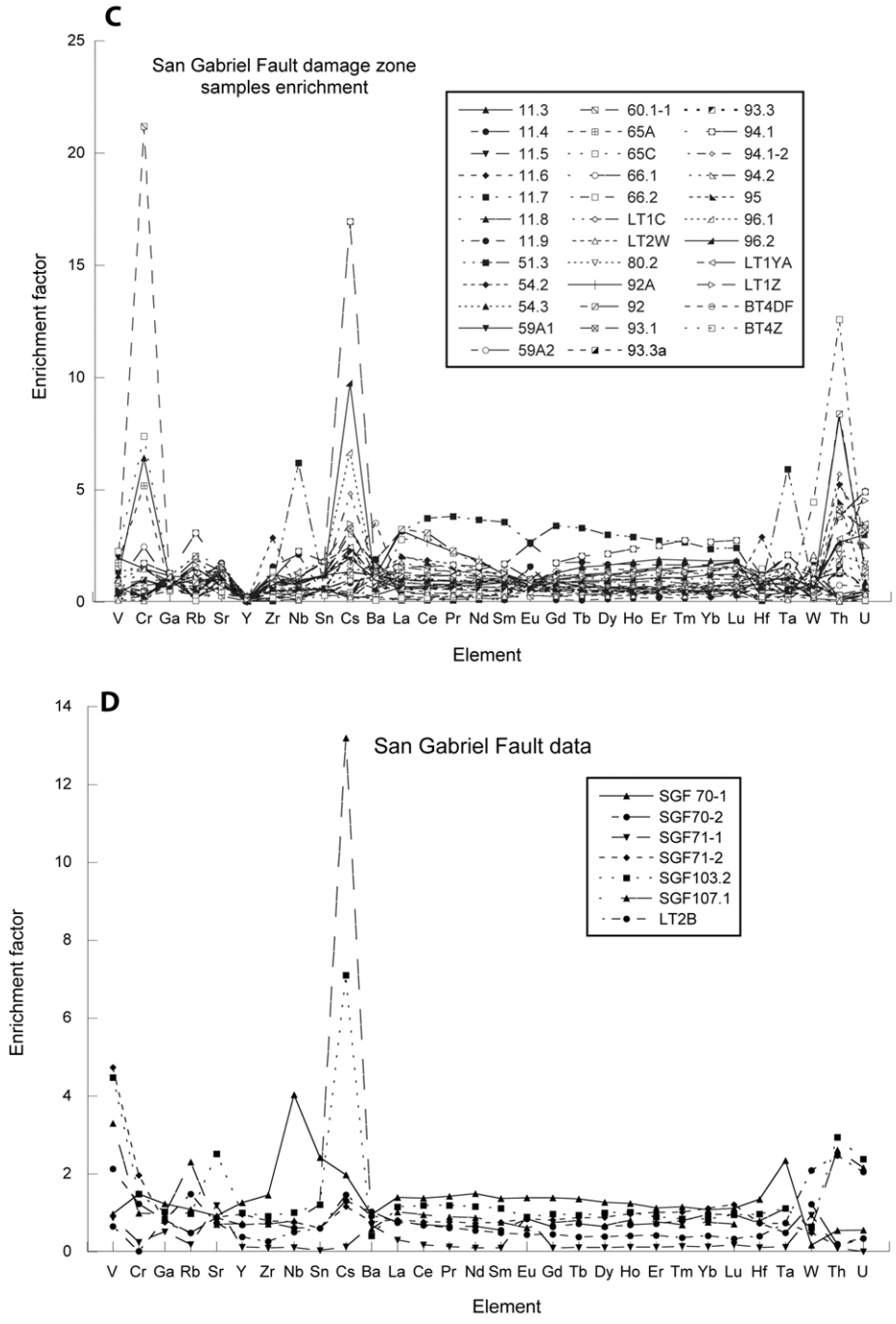

Figure 8. Rare earth and trace element enrichment data for samples from the damage zone and fault zone rocks of the San Andreas and San Gabriel Faults. A) Data for damage zone rocks from the San Andreas Fault. Slight enrichments in Rb, Sr, and Nb, significant enrichments in Cs and Th, and depletion in Sm are observed. B) Data for damage zone rocks from the San Gabriel Fault. Slight enrichments in Rb, Sr, Nb, and significant enrichments in V, Cs, and Th are observed. C) Data for the San Andreas Fault gouge samples. Slight enrichments in Rb, Sr, Nb, Hf, Ta, and significant enrichments in V, Cs, and Th are observed. D) Data from the San Gabriel Fault gouge samples. Slight enrichments in Rb, Sr, Nb, Hf, Th, and significant enrichments in V and Cs are observed.

The bootstrap analyses of the whole-rock data enable us to examine the variations within, and differences between, the different rock types. The San Andreas Fault data (Figure 6) show that the damage zone rocks are enriched in Ca and loss on ignition components relative to the granodiorite and quartzo-feldspathic protoliths (Figures 6b and d), and higher in iron than the QFP rocks (Figure 6a). The San Gabriel Fault samples show that the most notable signatures are LOI values that are consistently higher in the damaged zone and principal slip zone rocks than in unaltered protolith (Figure 7), and SiO_2 and K_2O values that are relatively depleted in damaged rock (Figure 7). The CaO, Fe_2O_3, MgO, MnO, and LOI values are consistently higher in the granodiorite damage zone compared to the granodiorite protolith (Figure 7). The CaO, MgO, and LOI values are consistently enriched, and Fe_2O_3 is generally enriched with some outliers in the gneissic damage zone when compared with the amphibolite and quartzo-feldspathic protolith. The volatile component of the damage zone rocks is 2-5x higher than in the protolith, likely indicating that fluid-rock interactions occurred in the damage zone.

Trace and rare-earth element data provide further insight into the geochemistry of the fault-related rocks and track relatively similarly for the different rock types (Figure 8; Supplemental Figure 1). We directly compare values from different types of rocks across the fault zones, by comparing the samples from deformed and sheared rocks with reference protolith values. We determine the mean values of a regional protolith from 16 samples of quartzo-feldspathic gneiss and amphibolite gneiss (Table 3) and normalize our data concerning this local standard:

$$Enrichment\ factor = \frac{\text{deformed rock value}}{\text{protolith value}} \quad (1)$$

The rocks from the damage zone of the San Andreas Fault are enriched in Sr, Nb, Cs, and to a lesser extent, Rb, and Th, and depleted in Sm relative to the local protolith; the fault gouge rocks are enriched in Sr, Rb, Cs, Hf, Ta, and Th. (Figures 8a and b). Damage zone rocks of the San Gabriel Fault zone are enriched in Cr, Nb, Cs, Ta, and Th, and samples from the principal slip zones are high in V, Rb, Sr, Nb, Cs, Ta, and Th (Figures 8c and d).

3.3. X-ray Fluorescence Maps

The combination of the analysis of deformation textures with the nature of alteration assemblages and carbonates in the fault-related rocks (Crouch, 2022; Studnicky, 2021), and the whole-rock geochemistry indicate that at the drill core, thin-section, and 2-g sample scales, the deformed rocks experienced moderate to significant amounts of alteration and mineralization during fault development. The XRF-based elemental mapping helps to determine the grain-scale nature of this alteration and its relationship to deformation textures.

The textures and element distribution in the damage zone rocks (Figures 9-16) reveal micron-scale variations and concentrations of transition elements in the deformed rocks. Protolith plagioclase and K-feldspar grains in the damage zones are altered and fractured, and narrow zones of cataclasite cut the rock. Rocks that reflect early or lesser stages of deformation in both fault zones (Figures 9 and 10) contain mm-thick transgranular fractures and slip surfaces (Figure 9a) that weave through the fractured protolith feldspar grains (Figures 10 b-e; 11). In places, fractures are at high angles to these surfaces (Figure 10a) and filled with cataclasite. Thin fractures emanate from some slip surfaces with sharp tips. The slip surfaces are composed of rounded clasts in a very fine-grained matrix enriched in Fe, Mn, Ti, and Cr. Planar intragranular fractures in plagioclase grains are enriched in these elements, and in some places significantly enriched (see, for example, the Ti, Mn, and Cr maps in Figure 9 b). These metal element-filled cross fractures define smaller angular grains that define angular fragments. The trace elements Ti, Mn, and Cr are thin planes that are finely distributed in thin surfaces and mm-scale pods (Figure 10b). The damage zone sample from the San Gabriel Fault is a relatively undeformed sample at the drill core scale. Yet in the XRF maps, the distribution of Cr, Mn, and Ni indicate the presence of fractures in the feldspar-rich sections (Figure 10b). These relationships continue in more deformed rocks.

The nature of fractures and elemental redistribution in brittle deformed rocks and the transition from protolith to faulted rocks can be seen in the XRF maps. Fracture networks that form adjacent to and within small-displacement faults (Figure 11) are marked by significant iron concentrations that link iron-rich areas to the networks (Figure 11b). Calcium is also distributed in the fracture networks (Figure 11c), and Fe permeates the rocks at the sub-mm scale (Figure 11e). The anti-correlation between Ca and Fe is clear (Figure 11f), and some of the Ca appears to be in elongated zones in the fault. The maps show that the fragments in the faults are bound by added Fe, Ca, and other trace elements.

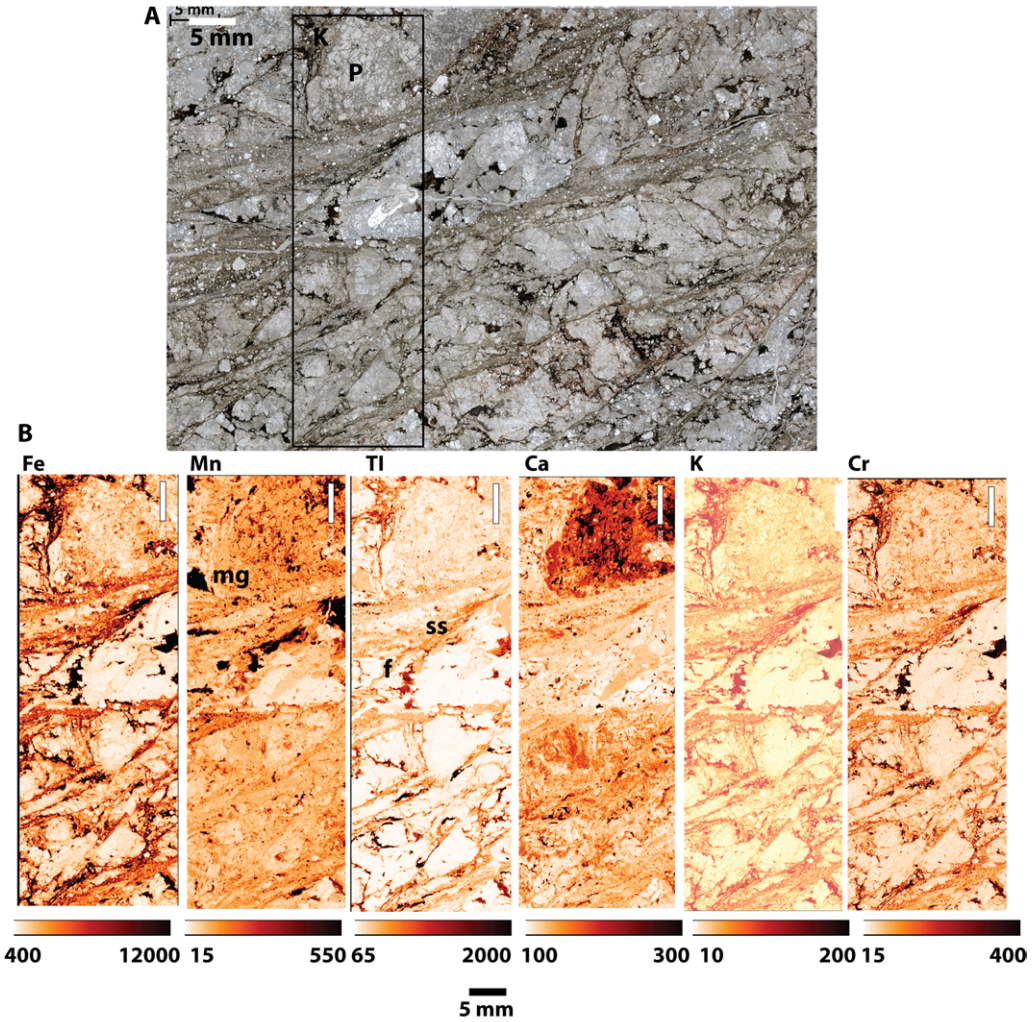

Figure 9. Microstructures and elemental distribution in sample LE 2-355 of the San Andreas Fault damage zone, Lake Elizabeth site. See Figures 2A and 3A for the location of this sample. A) Plane-polarized light photomicrograph of the sample (see Figures 2A and 3A for location). The rectangle indicates the region examined with XRF mapping. The plagioclase feldspar (P) and potassium (K) grains in the protolith are altered and fractured, and narrow zones of cataclasite cut the rock. B) Elemental maps for Fe, Mn, Ti, Ca, K, and Cr across part of the sample. Iron is distributed in the sheared rock with Ti and appears to originate from equant magnetite grains (mg) that have small amounts of Ti, Mn, and Cr, and alteration of mafic grains. Slip surfaces (SS) cut the sample and are composed of clay-rich cataclasite. Cataclasite zones are highly enriched in Fe, Mn, Ti, and lesser Cr; thin bands enriched in these elements follow fractures between shear zones. Iron is distributed through the sheared and fractured rocks, and the Ti, Mn, and Cr distribution along fractures, either as nearly continuous linings in the TI and maps, or as small, concentrated blebs (Cr) defines the intragranular fractures, sheared zones, and intragranular fractures in feldspars. Zones of high Fe-Ti-Mn-Cr concentration are connected to sheared rocks via 'feeder' fracture f. Fine-scale fracture networks in feldspars (FN) are defined by metal concentrations.

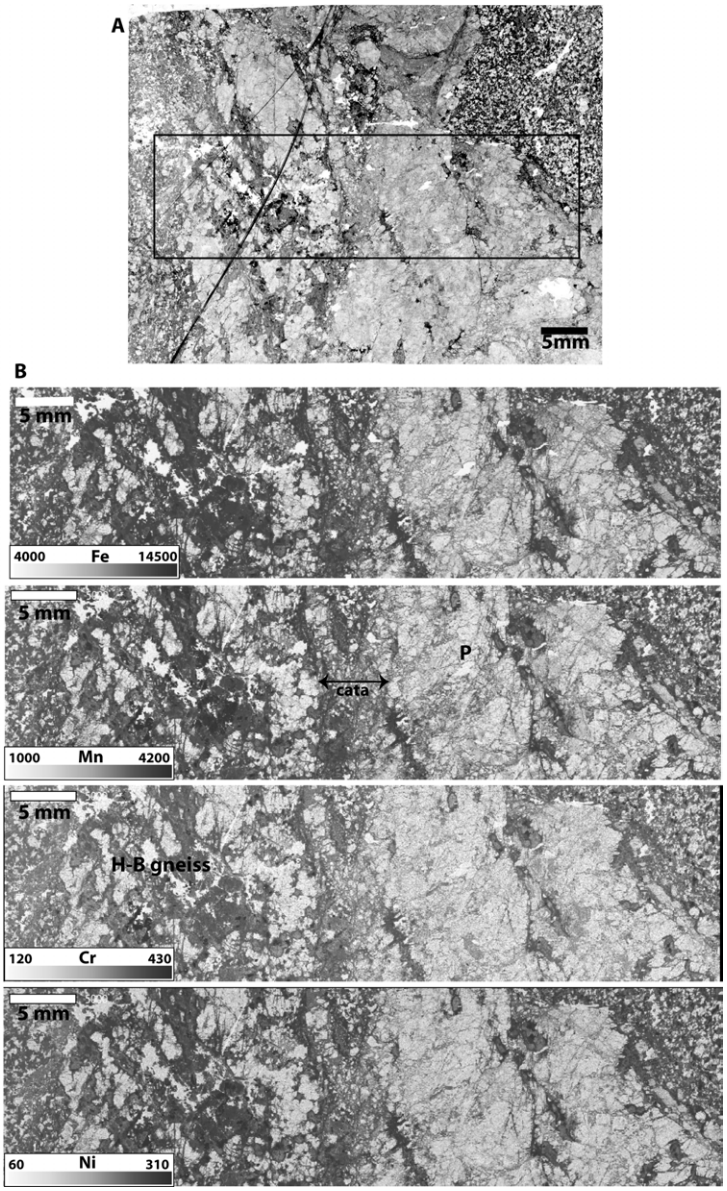

Figure 10. Microstructures and elemental distribution in sample SGF 51.1 of the San Gabriel Fault damage zone, See Figures 2B and 3E for the location of this sample. A) Plane-polarized light photomicrograph of the sample. The rectangle indicates the region examined with XRF mapping. B) Elemental maps of a portion of the sample for Fe, Mn, Cr, and Ni. Coarse foliation and concentrations of mafic mineral and feldspar-rich regions in the foliated gneiss are cut by an incipient fault on the right side of view. The sample is from the damage zone of the fault and shows the nature of the transition from primary hornblende-biotite gneiss (H-B gneiss) to a cataclasite zone (cata) and diffuse Fe-Mn-Cr-Ni lined fractures distributed throughout the plagioclase grains (P). Iron-rich regions map the location of hornblende and biotite in the gneiss, and several concentrated zones in the plagioclase zones (P). Mn mimics the iron distribution and defines the fracture networks and Fe and Mn define incipient distributions in the fractures in feldspars. Densely, closely spaced fractures in feldspars are marked by the Mn, Ni, and Cr maps. The Cr and Ni maps show the co-location of these trace elements with the iron and Mn in the less deformed rocks, and thin, filled fractures in the Ni maps define fractures.

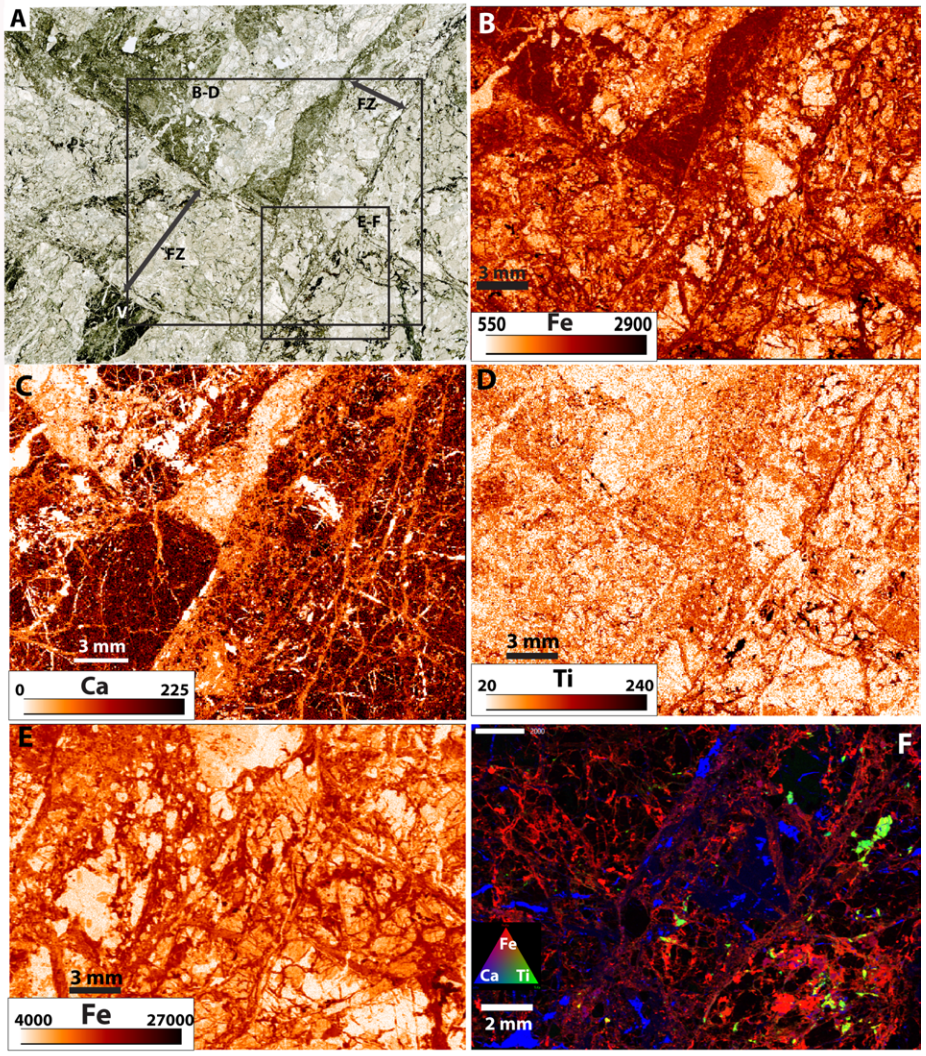

Figure 11. Microstructures and elemental distribution in sample SGF 71.1 from the San Gabriel Fault. A) Plane-polarized light photomicrograph of the sample (see Figure 2B and 3F for location). The sample contains intact and fractured feldspar and hornblende + biotite grains, some cut by calcite veins (V), and small fault zones (Fz) that intersect in the middle of the region mapped in Figures B-D) Rectangles indicate the region examined with XRF mapping. B) Iron map of the area shown in A) Iron is concentrated in primary gneiss grains and in fractures and fault zones. The Fe is concentrated along the edge of the right fault one, with angular feldspar fragments in the fault. shows the connection between iron-rich regions and the fractures in the fault zone (Fe). C) Calcium map shows the location of Ca-bearing plagioclase grains. D) The Ti map shows that it is concentrated in discrete narrow regions in this view. E. A magnified view of the region with the iron map reveals the fine-scale distribution of iron. F. Tricolor Fe-Ca-Ti map reveals the nature of the Fe distribution (red) in the host rock and into the fault zones either as sheared zones along fault edges or as irregular zones. The calcium (blue) is concentrated in thin elongate zones that suggest they are disarticulated veins fragments. Sub-equant titanium-rich grains (green) have experienced little alteration. The lack of Ca and Ti overlap suggests that Ti lies in rutile grains.

Samples that contain more well-developed slip surfaces and faults (Figures 12-14) reveal the significant concentration of the transition elements and the development of shear fabrics in the rocks. Transition element-lined fractures (Figure 12) document micron- to mm-scale fracture networks that define block-shaped fragments surrounded by the fractures. Regions that we infer are primarily Fe-oxide and amphibole-biotite grains are rare (Figure 12), and the Fe and Mn distributions create a 'feeder' texture where it appears that the iron-rich zones of the fractured protolith connect to the cataclasite zones. The cataclasite zones are enriched in Ca relative to the host rocks. The qualitative spatial correlations amongst the transition metals are quantified with correlation plots (Supplemental figures 2- 4) where Mn increases nonlinearly with Fe. Chromium and Ni increase with Mn in the sheared rocks.

The nature of highly sheared rocks, the impacts of zeolite and carbonate mineralization, and the apparent mobilization of transition elements are evident in samples from the San Gabriel Fault, where the fault exhibits a well-developed foliated shear zone (Figure 13). The sheared rocks are composed of very fine-grained clays, plagioclase, calcite, and zeolites (Crouch, 2022). Rounded lozenges of Ca-rich clasts are embedded in an iron-rich foliated zone and appear to be a rootless Type 2 superposed fold (Figure 13a). Elongate high birefringence lozenges are enriched in calcium and lie within iron-rich cataclasites (Figure 13b). The pattern of mineralization indicates that earlier calcite veins ± zeolite zones were incorporated into the shear zone, and the transition element distribution appears to be relatively homogenized in the sample, as seen by the frequency of pixels with similar Fe and Mn concentrations (Supplemental Figure 3). Iron, Ti, Cr, and Mn are concentrated in thin cataclasite zones embedded in altered damage zone rocks (Figure 12) of the SAF rocks.

Both faults exhibit very thin fault surfaces that suggest extremely localized slip and evidence for rapid slip. A sample from a relatively isolated 'secondary' fault north of the main fault zone (Figure 14) reveals a rich combination of microstructures and elemental patterns. The sample consists of several sub-mm thick slip surfaces (Figure 14 A, B) with significant concentrations of Fe, Mn, Ni, and Ti (Figure 14C). The relatively straight main slip surfaces lie within a fractured and cataclastic matrix, with short off-fault tensile fractures filled with the same material as the main slip surfaces. At high resolution, the iron-rich slip zone material appears amorphous with a finely laminated appearance and small rounded fragments in the material (Figure 14d). The iron-rich material in the fault surfaces does not exhibit clear grain boundaries, suggesting the material may have a melt origin.

Narrow slip surfaces may exhibit S-C shear fabrics (Figure 15) with extremely fine-grained, amorphous iron-rich fault fill defining sharp boundaries in a sample from the San Andreas Fault. Narrow slip surfaces

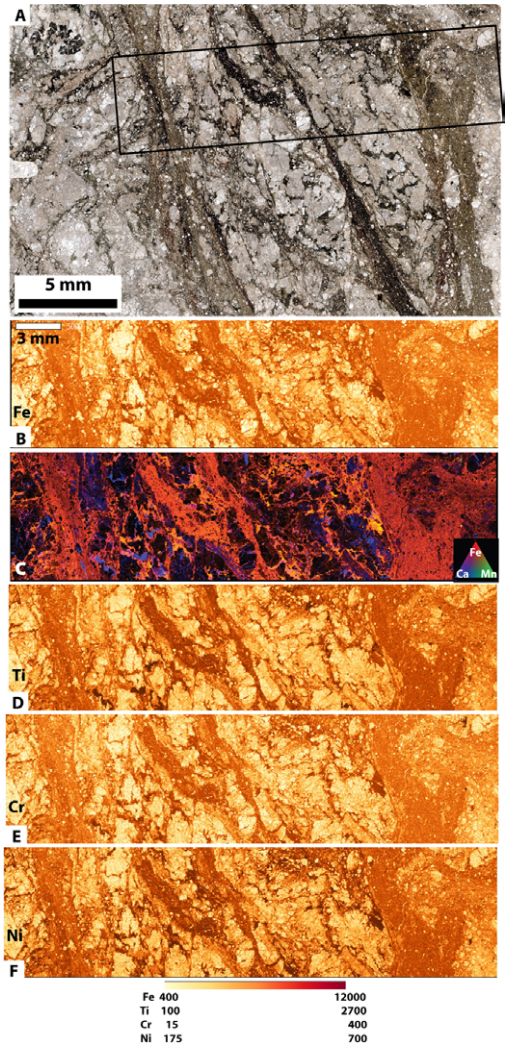

Figure 12. Microstructures and elemental distribution in sample LE 6-433 of the San Andreas Fault damage zone, Lake Elizabeth site. A) Plane-polarized light photomicrograph of thin section (see Figure 2A and 3B for location). This sample represents a more mature stage of fault development and represents a transition from fractured damage zone rocks to cataclastically sheared fault-related rocks. The rectangle indicates the region examined with XRF mapping. The sample consists of damage zone rocks dominated by plagioclase, three cataclasite zones, and a thin slip surface marked by optically opaque materials. B) Elemental maps of a portion of the sample for iron. The sheared cataclasites are rich in Fe, Mn, Ti, Cr, and Ni – see Figure 12 C, D, E, and F) often as zones comprised of very fine-grained cataclasite. In some zones a compositional layering is evident. C) Tricolor map of Fe (red) Mn (green) and Ca (blue) shows that iron dominates the cataclasite zones, and Ca, likely as calcite, occurs as small irregular zones that are likely disarticulated calcite veins. The maps of metals D) Ti, E) Cr, and F) Ni mimic the Fe patterns. Fractures and sheared zones are irregular and connect to equant grains. Likely magnetite grains (black) are altered and Fe+Ti+Cr+Mn are distributed in irregular fractures that are connected to the magnetite. Fractures in the feldspars are lined with transition elements and define angular to subangular fragments.

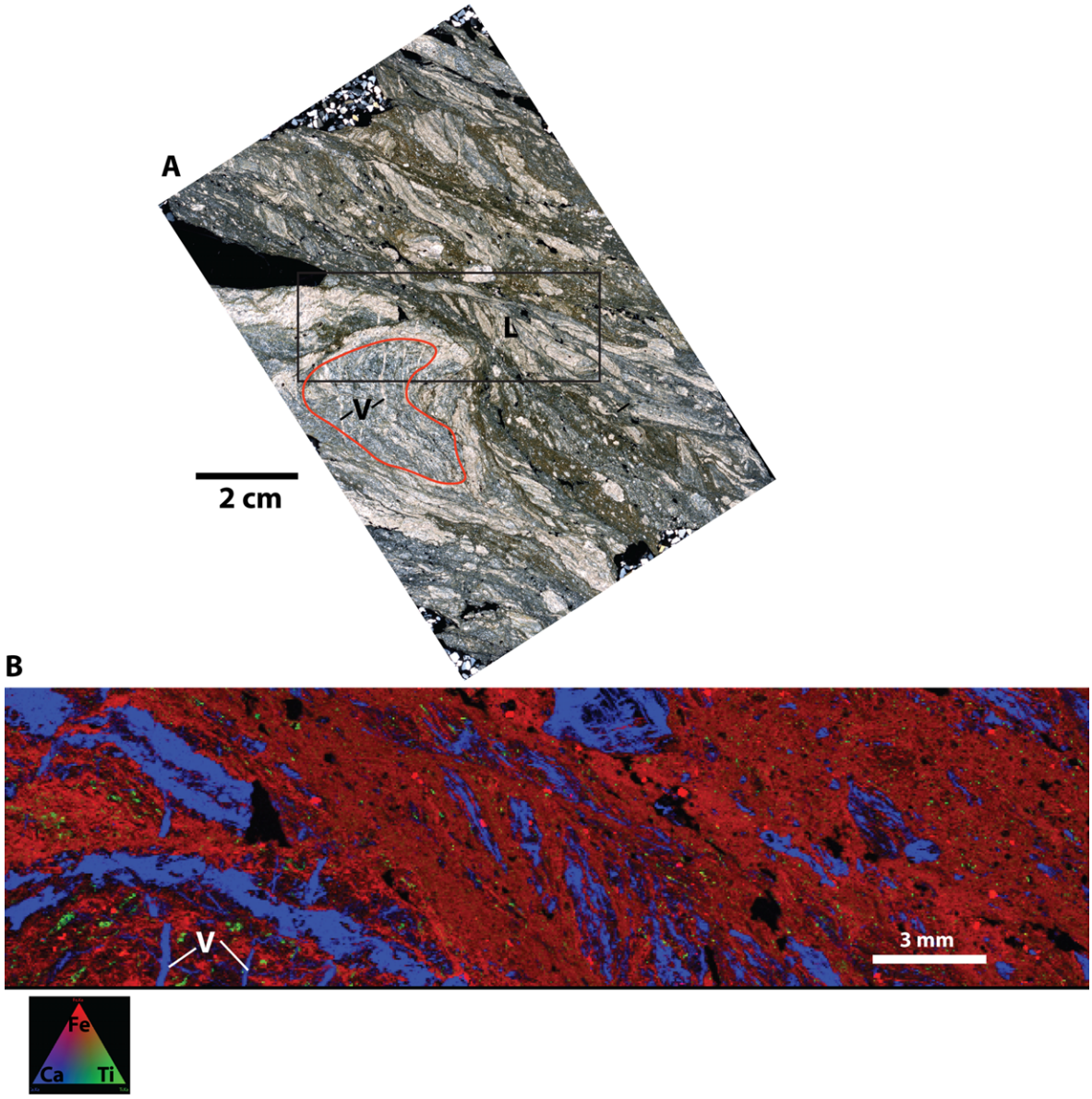

Figure 13. Microstructures and elemental distribution in sample SGF 65A from the San Gabriel Fault. A) Plane-polarized light photomicrograph of the sample (see Figure 2B and 3G for location). The rectangle indicates the region examined with XRF mapping. The sample demonstrates the nature of highly sheared calcite and zeolite mineralized zones. Calcite lozenges and very fine-grained foliated cataclasite define foliation, with folded/rolled veins. B) Tricolored elemental map for the detailed region. Iron (red) and Mn are relatively uniformly distributed through the fine-grained sheared rocks. Ti (green) occurs as small flecks in fine-grained sheared rocks. Ca is concentrated in elongated lozenges in the sheared rocks and as short thin planar sites as veins (V). The large, rounded region that we interpret as a rootless fold (red line) consists of a calcite-rich rim and a fine-grained matrix of cataclasite and possibly zeolites, which are themselves cut by thin straight calcite veins. Calcium-rich rounded-to-elongate zones are entrained in the fine-grained Fe-rich cataclasite.

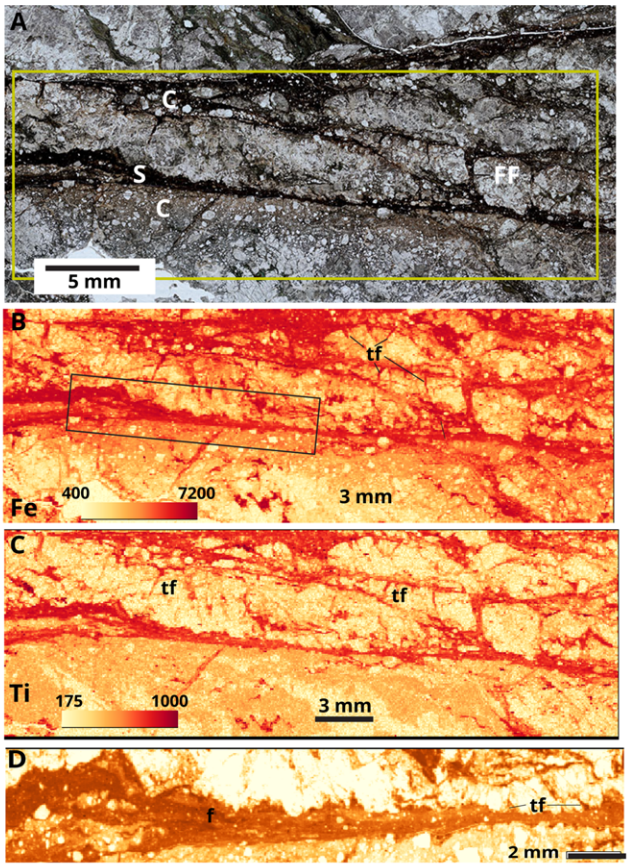

Figure 14. Microstructures and elemental distribution in sample LE 6-134 of the San Andreas Fault damage zone, Lake Elizabeth site. A) Plane-polarized light photomicrograph of the sample (see Figure 2A and 3C for location). The rectangle indicates the region examined with XRF mapping in C and D) Sample contains 50 mm to 1 mm thick black, optically opaque slip surfaces (S) along and within cataclasite zones (C). The central zone is bounded by a straight boundary on one edge and an irregular wavy contact above. In several places, sharp-filled fractures (FF) formed at high angles to the slip surfaces. B) Plane-polarized light photomicrograph of the sample. The numerous thin, filled fractures that appear to emanate from the main slip surfaces resemble off-fault tensile fractures. C) Elemental maps for Fe and Ti reveal fine-scale texture within the sample. Slip surfaces are marked by concentrations of Fe and Ti and Ni, Cr, and Mn – see Appendix). Tensile fractures (TF) from the slip surface are marked by Fe + Ti + Cr + Mn. Fractures at high angles to the slip surface define angular fragments between the slip zones. The upper fault is enriched in Fe + Ti + Cr + Mn and consists of cataclasite with tensile fractures filled with injected cataclasite. D) High-resolution magnified image of part of the lower slip surface. Data is processed with a 3-pixel window moving average window. In this map, the slip zone exhibits amorphous, foliated Fe (f) that is in the ~50 to 500 mm thick zone. 10-40 mm rounded fragments of host cataclasite are suspended in the Fe-rich material. Small wedge-shaped tensile fractures (f)appear to have been injected (I) into the adjacent damaged rocks and cataclasite.

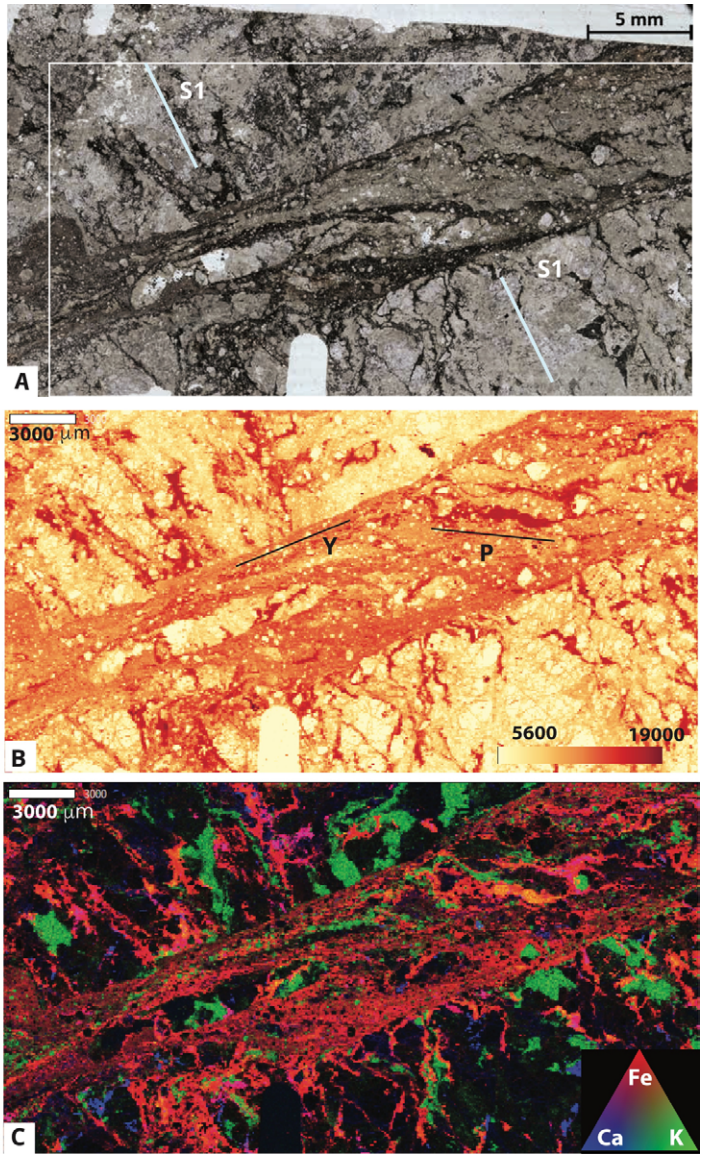

Figure 15. Microstructures and elemental distribution in a magnified part of a thin fault sample from LE 4-130. A) Plane-polarized light photomicrograph of the sample with primary foliations (S_1) cut by a zone of narrow shear surfaces. The rectangle shows the area examined in the XRF map. B) The foliated cataclasite sample consists of amorphous Fe-rich material with rounded calcium-rich clasts in it. The iron-rich fractures below the fault are cut off and some of the iron is entrained in the fault; small, rounded clasts of feldspar lie in the fault zone. The sample exhibits a crude Riedel shear geometry, with a Y-P- and X fabric indicating a top to the left sense of shear. Remnant clasts of Ca-rich protolith (blue and green) are parallel to the S fabric, and a secondary fabric dips more steeply. Irregular iron-rich zones in the fault zone of higher concentrations may be derived from altered and deformed mafic minerals, similar to Fe-rich zones below the fault. C) Tri-color Fe (red) K (green) and Ca (blue) plot of the shear zone. Primary K-rich zones in the protolith are K-feldspars, which are elongated and distributed within the shear zone. Calcium occurs as small spots in the sheared zone. The shear zone is also enriched in Ti, Cr, and Mn.

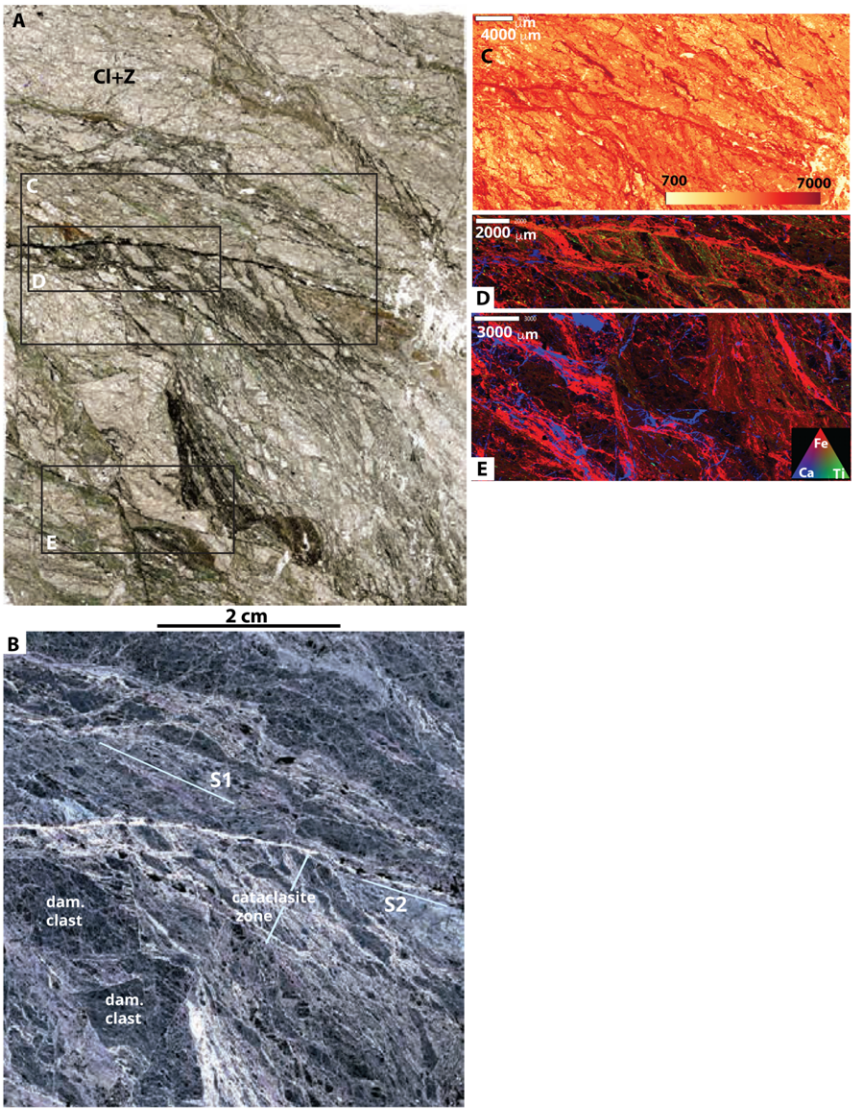

Figure 16. Microstructures and elemental distribution in sample SGF 96.1 from the San Gabriel Fault. See Figures 2B and 3I for the location of this sample. A) Plane-polarized light photomicrograph of the sample (see Figure 2B and 3I for location). The rectangle indicates the region examined with XRF mapping. The sheared rock consists of zeolite+ clays (Cl+Z) and dark iron-rich zones that define the foliation, and which may define a pressure solution seam. The clay + zeolite shear zone is cut by cataclasite zones (cata), in which the fragments consist of the 'host' sheared material. B) Cross-polarized light image with a blue filter shows that the cataclasite zone is bounded by a thin seam enriched in Fe, Mn, Cr, and Ni, and may indicate the presence of a pressure solution seam. Faint outlines of damaged clasts (dam. clast) are seen in the sheared zone defined by the foliation (S1). C) XRF Fe map of the sheared rock. D and E. Tricolor Fe (red) Ti (green) and Ca (blue) of two sites. Fe defines the seams, Ti is distributed through the sheared rocks, and Ca is very finely disseminated. In the region outlined in E, Ca lies in elongated zones parallel to the foliation and small sites at high angles to the foliation.

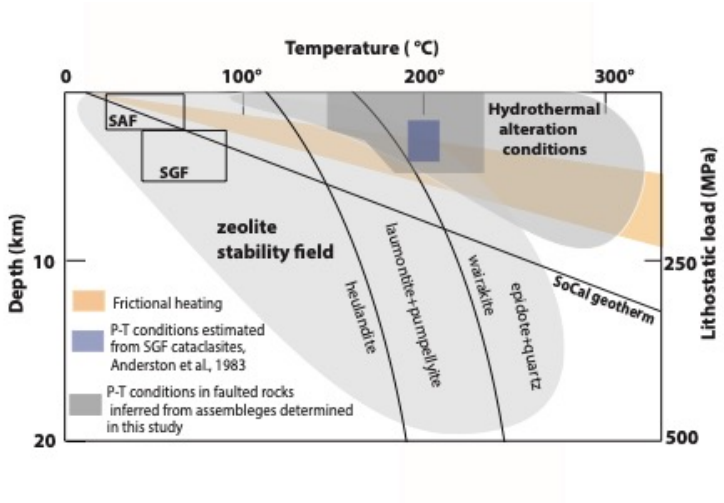

Figure 17. A conceptual model for conditions in and around the fault zones, and development of hydrothermal alteration assemblages in shallow portions of the San Andreas and San Gabriel Faults. The P-T conditions and stability field adapted from Anderson et al., 1983; Evans, 1988; Evans and Chester, 1995; Weisenberger and Bucher, 2010; Utada, 2001. The rectangles labeled SAF and SGF are the likely P-T conditions with ambient geotherm P-T conditions. The hydrothermal alteration field represents the conditions under which free fluid phases could migrate in the fractured and faulted crystalline rocks in the upper crust and fluids would be at least partially oxidizing. In this region fluids can transport heat and solutes, and in crystalline rocks, this flow regime permeability would be dominated by the presence of fractures and faults. At higher temperatures and pressures these fluids would evolve to 'metamorphic' fluids that react locally, are less able to migrate in fracture-dominated crystalline rocks, and drive higher-grade metamorphic reactions. The SoCal geotherm is based on Lachenbruch (1986), and Buscher and Spotila, (2007). The zone of fault-related frictional heating indicates the likely range of temperatures based on frictional heating calculations of Turcotte et al., 1980; Lachenbruch, 1986, for a range of coefficients of friction. The boxes labeled SAF and SGF indicate the pressure-temperature ranges for the fault-related rocks examined here, for present and ancient conditions. In these conditions, low-temperature zeolite phases are stable, but laumontite, wairakite, and epidote are not stable. Fault-related mineral assemblages documented here and in Anderson et al, 1983, and Evans et al., 1995 are consistent with externally derived hydrothermal fluids and/or fault-related heating and deformation that produce mineralization in the shallow portions of the faults.

cut well-defined protolith fabrics. The amorphous and foliated nature of the narrow slip surface suggests extreme comminution or melt along these surfaces.

In the San Gabriel Fault, extremely narrow slip surfaces are marked by concentrations of fine-grained clay-zeolite-carbonate-rich sheared rocks (Figure 16). The highly sheared, very foliated clays, carbonates, zeolites, and iron oxides are brecciated and cut by 5-20 um thick surfaces defined by concentrations of Ni (Figure 16B), Ti, Cr, and As. The nature of these dark surfaces suggests that these might be the result of pressure solution that is superposed on the shearing and brecciation.

4 Analysis and Implications

We document evidence of mineralogic alteration associated with the deformation in the shallow parts of the San Andreas and San Gabriel fault zones. The mineralogic data (Crouch, 2022; Crouch et al., submitted; Evans and Chester, 1995; Studnicky, 2021; Studnicky et al., submitted; Williams et al., 2021) show that the fault-related rocks of both fault zones are composed of damage zone rocks within fault zones that exhibit the results of a large amount of shearing. The mineralogy of the deformed rocks and whole-rock geochemical analyses (Figures 5 and 6) document moderate degrees of alteration. Loss on ignition values are as much as 6%, compared with protolith values of ~1-2%. The increased values for the loss on ignition content are most likely a measure of the effects of H_2O and CO_2- bearing fluids. The rare earth and trace element chemistry, and the textures of the rocks observed in thin sections with visible and X-ray light, point to the alteration processes that include the degradation of K- and Na-Ca bearing feldspars and the subsequent development of clay. The development of zeolites is documented by the Cs enrichment, deposition of calcite, alteration of hornblende, biotite, and iron oxides to chloritic minerals, and the migration of transition metals in the deformed rocks.

We suggest that the alteration signal from the whole rock and XRF mapping data show that migration of the transition elements into fractures and then to fault gouge is a signature of hydrothermal fluids interacting with iron and manganese in the protolith. Manganese, a trace element in most mafic minerals (0.1-0.2 wt. % of the amphibolite gneiss, and comprises ~0.1 – 0.2 wt% of the quartzo-feldspathic gneisses in Tables 1 and 2), typically substitutes for iron. We observe correlations amongst Mn, Cr, and Ni in a number of the samples examined here (Supplemental Figures 2-4), and thus the Cr signature in the trace element data is a proxy for the effects of Mn and the mobility of other transition elements such as V, Co, Cu, and Zn. The MnO_2 tends "scavenge" transition elements (Jenne, 1968).

The trace element distribution patterns (Figure 8) can be sorted into four broad categories. The Cs, Rb, and S are large ion lithophile elements that are often related to alteration and hydrothermal alteration (see for example, Rumbiak et al., 2021). We interpret these element enrichments as due to feldspar alteration that liberates K (and traces of Rb and Sr), zeolite development associated with Cs enrichment (Goguel, 1983), and hydrothermal alteration and mineralization in the fault zone. The V and Cr enrichment (and by association, Fe, Ni, Ti, Zn, and Mn examined in the XRF maps) is a signature of alteration and/or mineralization due to local metal transport within the fault zones. The Nb, Hf, Ta, and Th signatures are likely the result of the preservation of high-field strength elements in the faulted rocks, perhaps due to some volume reduction in the fault zones. The Th enrichment may reflect this volume loss, as U/Th values are lower in the deformed rocks. Here U, a common mobile trace element in carbonates (Sturchio et al.,

1998; Timofeev et al., 2018), may be removed from some of the trace element samples, creating a relative enrichment in Th-damaged rocks.

We infer that hydrothermal fluid-rock interactions facilitated the majority of the alteration in the fault zone (cf., Callahan et al., 2020). The presence of alteration phases epidote, and calcite + laumontite indicate temperatures ≤ 250°C (Utada, 2001; Ferrill et al., 2004; Figure 17), above the current and temperatures of both fault zones and likely above the ambient temperatures for a San Andreas Fault zone reconstructed for the ~ 1-2 km maximum uplift (Spotila et al., 2002) and at the lower temperature range for a reconstructed San Gabriel Fault (Evans and Chester, 1995; Blythe et al., 2002). Laumontite is common along and within the San Andreas Fault and its exhumed predecessors, is stable within the temperature range of ~50 – 230°C (Utada, 2001), and appears in many parts of faults from the San Andreas Fault system (James and Silver, 1988; Blenkinsop and Sibson, 1992; Evans and Chester, 1995; Weschler et al., 2011, Forand et al., 2014; Crouch and Evans, in revision). Calcite veins and cement are evidence of fluid-assisted healing within the fault damage zone. Twinned calcite cement in pulverized rocks, in which intra-granular fractured rocks recover some of the lost strength of the damaged grains via cementation, indicates that precipitation of calcite was followed by added loading in the fault zone. Calcite twins can occur at temperatures as low as ~20°C (De Bresser and Spiers, 1997; Ferrill et al., 2004). Twinned, i.e., aseismic, calcite veins were subsequently cut by brittle fractures filled with precipitated zeolite. The calcite grains with optically measurable twins indicate a temperature range of ≥20°C to ≤250°C with the high density and morphology of the twinning likely indicating temperatures closer to ~170°C - 200°C (Ferrill et al., 2004). The mechanical twinning and subsequent brittle fracturing provide evidence for aseismic to brittle transitions as well as alternating fluid flow events. The cross-cutting relationships, especially in the San Andreas Fault samples (Studnicky et al., submitted), suggest that the alteration assemblages are formed by repeated interactions with similar composition fluids that mobilize the rare-earth, trace, and carbonate elements.

Our work documents the utility of integrating X-ray-based elemental mapping with other microscopy methods to decipher the alteration and deformation in brittlely deformed rocks. The high-resolution elemental maps of the transition elements in these rocks in almost all cases show concentrations of Fe, Mn, and depending on the samples, Ti, Cr, or Ni in the narrow fault zones, the foliated cataclasites, and the filling of small fractures in the damaged host rock (Figure 9-16). These metals, mobile in their oxidized states, are mapped in rocks with little deformation over 10's cm (Figure 4) down to the grain scales (Figure 9) and are a common feature of highly sheared rocks. We posit that the hydrothermal fluids, moving through the host rock and the fractured rocks pick up these major, minor, and trace elements from the

amphibole, biotite, and trace minerals such as rutile and titanite, and distribute them in multiscale fracture networks. As the faults evolve (Figures 11 and 13) carbonate mineralization occurs as well, and the fault zones record these alteration processes.

The optical microscopy, X-ray diffraction mineralogy, whole-rock chemistry, and X-ray elemental mapping results presented here all indicate that the fault-related rocks in the San Andreas and San Gabriel Faults experienced significant amounts of chemical and mineralogic alteration during deformation. Moderately indurated zones of Fe- and Mn-rich chloritic, clay, and zeolite minerals appear to have formed early in the history of fault slip and were reworked in the fault zones as they developed. Mineralization and alteration are associated with fracture systems observed at the ~10 m scale (AMEC FosterWheeler Plate 7, LADWP; CHSRA report) to the sub-millimeter scales. These fractures appear to facilitate fluid migration into the rocks and alteration and mineralization within the fault zones. This led to the generation of low-frictional and bulk elastic strength rocks.

The data presented here, and the work of others on the San Andreas Fault system (Anderson et al., 1983; Bradbury et al., 2015; Chester et al., 1993; Forand et al, 2014; Gratier et al., 2011; Holdsworth et al., 2011; Moore and Rymer, 2012; Richard et al., 2014; Schulz and Evans, 2000) and other faults (Boulton et al., 2017; Callahan et al., 2020; Faulkner et al., 2003; Holdsworth et al., 2011; Jeffries et al., 2006; Kaduri et al., 2017; Niemeijer et al., 2012; Smith et al., 2013; Towend et al., 2017; Wibberley et al., 2008) indicate that seismogenic faults are strongly influenced by diffusive mass transfer, hydrothermal, and mineralization processes that alter the chemical and physical properties of the fault-related rocks. Most of these processes are active for over 100's or 1000's+ years, probably during the interseismic part of the seismic cycle, while rapid seismic slip ruptures through these rocks along narrow, fine-grained slip zones.

Conclusions

We interpret geochemical data from deformed rocks associated with the San Andreas and San Gabriel Fault zones to show that the rocks in the damage zone of these two faults experienced significant hydrothermal alteration synchronous with brittle deformation. Fault-related alteration of tonalite gneisses to zeolites + calcite + clays + chlorite ± hydrous phyllosilicates ± epidote in brittle and semi-brittle deformed random-fabric cataclasites, foliated cataclasites, phyllonite, and ultracataclasite shear zones. This produced fault damage zones up to 300 m thick that consist of rocks significantly weaker at the grain- to meter-scale relative to the host rocks, with abundant microfractures and mesoscopic shear surfaces.

The fault-related alteration within the damage zone indicates a temperature regime of up to ~250°C, a fault zone of reduced strength, with an at times open, permeable fracture system facilitating the fluid flow

and element mobility, reduced permeability within gouge, and high concentration of low-seismic velocity minerals. The ample zeolite and calcite alteration in the fault-related rocks change the host rock rheologic properties, the permeability and porosity of the damaged rocks, and, through cementation, recover some rheologic strength lost in previous rupture events.

The high degree of induration and lack of 'incohesive' fault-related rocks in these rocks may be attributed to the distribution of calcite and zeolite cement and veins, and the development of fine-grained clay and Fe-Mg oxide sealed fractures, which are facilitated by the damaged structure and fluid pathways in the fault zone. The brittle fractures increased the surface area of minerals available to mobile fluids to react, promoting alteration and mineralization. Although these mechanisms lead to fault weakening, the subsequent precipitation of veins and cement decreases the fault zone permeability (Figure 17) and increases its strength.

The variable induration exhibited in the rock indicates that thermal 'healing' created regions of moderate V_p and V_s rocks within zones of low-velocity, highly damaged rocks at shallow levels. Hydrothermal alteration at these relatively shallow levels suggests the damage zones experienced the advection of hydrothermal fluids or the in situ heating of fluids from the frictional heating within the fault zones (Jacobs et al, 2006; Shipton et al., 2006). These processes produced shallow damage zones that may be significantly weaker than the protolith during some stages of the fault cycle and produced many potential surfaces for slip during and after a major earthquake. Over time, mineralization may serve to partially heal the fault-related rocks, producing intermediate-strength fault zones and thereby influencing slip accommodation in the shallow crust.

Acknowledgments. Many thanks to Dr. Kate Scharer for alerting us to the LADWP and CHRSA site investigations, and for introducing the scientific community to these valuable data sets. This work is funded by an NSF grant 1824852 and SCEC grant 18077 to Evans; by the Geological Society of America - Continental Scientific Drilling Division Grants to Crouch and Studnicky, an American Association of Petroleum Geologists L. Austin Weeks grant, a Utah State University's Academic Opportunity grant, URCO grant, Peak Summer Research Fellowship, and a College of Science mini-grant to Kaitlyn Crouch; Caroline Studnicky was supported by the Geological Society of America - Graduate Student Research Grant 2020; a Utah State University - J. Stewart Williams Graduate Fellowship Spring 2019; Utah State University - Summit Scholarship Spring 2020; and an Association of Women Geologists - Salt Lake Chapter Research Grant 2019. Microscopy that guided the XRF mapping was performed at McGill University with the guidance of Dr. Christie Rowe and Dr. Jamie Kirkpatrick with funding from Fonds de Recherche du Québec, Bourses

d'Excellence Pour Étudiants Étrangers Assistance. Access to the SAF drill core and borehole log data was provided by Chris Heron of the Los Angeles Department of Water and Power. Many thanks to Dr. Christie Rowe and Dr. Randy Willams for discussions regarding this work. Access to the CHSRA core was provided by Kathlien Red (Kleinfelder) and Randy Anderson (CHSRA) in 2019, and Paul Guptill (Kleinfelder) and the California High-Speed Rail Authority provided access to borehole data from the borehole released under the California High-Speed Rail Public Records request # 22-164, October 2022. Use of the Stanford Synchrotron Radiation Lightsource, SLAC National Accelerator Laboratory, is supported by the U.S. Department of Energy, Office of Science, Office of Basic Energy Sciences under Contract No. DE-AC02-76SF00515. The SSRL Structural Molecular Biology Program is supported by the DOE Office of Biological and Environmental Research, and by the National Institutes of Health, National Institute of General Medical Sciences (P30GM133894). The contents of this publication are solely the responsibility of the authors and do not necessarily represent the official views of NIGMS, NIH, or DOE.

Author Contributions

Kaitlyn Crouch, Caroline Studnicky, and James Evans sampled the core in 2018 and 2019. Crouch and Studnicky examined the drill core in detail, recompiled the fracture spacing and borehole data from the performed microstructural studies that guided the geochemical studies, performed the X-ray diffraction studies, and compiled and curated all of the data sets, including optical microscopy images of the core samples. Crouch and Evans performed the XRF analyses of San Gabriel and San Andreas samples at SSRL in collaboration with Sharon Bone and Sam Webb in February 2020, and Sharon Bone examined San Gabriel samples via remote protocols in the autumn of 2020 in collaboration with Crouch and Evans. Evans, Bone, Edwards, and Webb performed the XRF analyses of San Andreas samples in 2018, and Evans, Edwards, and Webb performed the mapping of the whole core samples. The data were reduced by Evans and Crouch with the MicroAnalysis Toolkit software (https://www.sams-xrays.com/smak) developed by Samuel Webb at the Stanford Linear Accelerator Center (SLAC). Evans conceived of the core-based studies and the analyses of the samples with XRF mapping methods and wrote this paper, based on MS.c. theses by Kaitlyn Crouch and Caroline Studnicky, with edits and revisions from co-authors.

References

Anderson. J.L., Osborne, R.H. and Palmer, D.F., 1983, Cataclastic rocks of the San Gabriel fault-an expression of deformation at deeper crustal levels in the San Andreas fault zone, Tectonophysics, v. 98, p. 209-240.

Andrews, D. J. 2005, Rupture dynamics with energy loss outside the slip zone, Journal of Geophysical Research, v. 110, B01307, doi:10.1029/2004JB003191.

Archuleta, R. J., 1984, A faulting model for the 1979 Imperial Valley earthquake, Journal of Geophysical Research, v. 89, p. 4559-4585, https://doi.org/10.1029/JB089iB06p04559.

Barth, A.P., Wooden, J.L., Tosda, R.M., Morrison, J., Dawson, D.L. and Hernly, B.M., 1995a, Origin of gneisses in the aureole of the San Gabriel anorthosite complex and implications for the Proterozoic crustal evolution of southern California. Tectonics, v. 14, p.736-752. DOI:10.1130/0016-7606(1995)107<0201:CCITPO>2.3.CO;2.

Barth, A.P., Wooden, J.L., Tosdal, R.M., and Morrison, J., 1995b, Crustal contamination in the petrogenesis of a calc-alkalic rock series: Josephine Mountain intrusion, California: Geological Society of America Bulletin, v. 107, p. 201–212. DOI: 10.1130/0016 7606(1995)107<0201:CCITPOO>>2.3.CO;2.

Bendat, J. S. and Piersol, A. G., 2000, Random Data, Analysis and Measurement Procedures, 3rd Edition, Wiley, New York, 2000.

Bergmann, U., Manning, P. L., Wogelius, R. A., 2012, Chemical mapping of paleontological and archeological artifacts with synchrotron X-rays, Annual Review of Analytical Chemistry, v. 5, p. 361-389.

Beyer, L.A., McCulloh, T.H., Denison, R.E., Morin, R.W., Enrico, R. J., Barron, J. A., and Fleck, R. J., 2009, Post-Miocene right separation on the San Gabriel and Vasquez Creek faults, with supporting chronostratigraphy, western San Gabriel Mountains, California: U.S. Geological Survey Professional Paper 1759, 27 p.

Blythe, A.E., House, M.A., and Spotila, J.A., 2002, Low-temperature thermochronology of the San Gabriel and San Bernardino Mountains, southern California: Constraining structural evolution, in Barth, A., ed., Contributions to Crustal Evolution of the Southwestern United States: Boulder, Colorado, Geological Society of America Special Paper 365, p. 231–250, doi:10.1130/0-8137-2365-5.231.

Boulton, C., Menzies, C.D., Toy, V.G., Townend, J. and Sutherland, R., 2017, Geochemical and microstructural evidence for interseismic changes in fault zone permeability and strength, Alpine Fault, New Zealand, Geochemistry, Geophysics, Geosystems, v.18, p.238-265, https://doi.org/10.1002/2016GC006588.

Bradbury, K. K., Evans. J. P., Chester, J. S., Chester, F. M., Kirschner, D. L., 2011, Lithology and internal structure of the San Andreas fault at depth based on characterization of Phase 3 whole-rock core in the San Andreas Fault Observatory at Depth (SAFOD) borehole, Earth and Planetary Sciences Letters, v. 310, p. 131-144, **https://doi.org/10.1016/j.epsl.2011.07.020**.

Bradbury, K.K., Davis, C.R., Shervais, J.W., Janecke, S.U. and Evans, J.P., 2015, Composition, alteration, and texture of fault-related rocks from SAFOD core and surface outcrop analogs: Evidence for deformation processes and fluid-rock interactions. Pure and Applied Geophysics, v.172, p.1053-1078, https://doi.org/10.1007/s00024-014-0896-6.

Brown, G. E., Jr., and Sturchio, N. C., 2002, An Overview of Synchrotron Radiation Applications to Low-Temperature Geochemistry and Environmental Science, in Applications to Low-Temperature Geochemistry and Environmental Sciences, Reviews in Mineralogy and Geochemistry v. 49 (1), p. A. Fenter, N. L. Rivers, N. C. Sturchio, and S. R. Sutton, eds., p. 1–115.

Bryant, W.A., compiler, 2017, Fault number 89c, San Gabriel fault zone, Newhall section, in Quaternary fault and fold database of the United States: U.S. Geological Survey, https://earthquakes.usgs.gov/hazards/qfaults.

Buscher, J. T., and Spotila, J. A. 2007, Near-field response to transpression along the southern San Andreas fault, based on exhumation of the northern San Gabriel Mountains, southern California, *Tectonics*, 26, TC5004, doi:10.1029/2006TC002017.

California High-Speed Rail Authority (CHSRA), 2019, Palmdale to Burbank Project Section, Preliminary Geotechnical Data Report for Tunnel Feasibility, Angeles National Forest, EEPB-KLF-TTK04-RE-0006_REV01 ANF PGDR, (https://hsr.ca.gov/high-speed-rail-in-california/project-sections/bakersfield-to-palmdale/), last accessed 4 October 2022.

Callahan, O.A., Eichhubl, P. and Davatzes, N.C., 2020, Mineral precipitation as a mechanism of fault core growth. Journal of Structural Geology, v.140, p.104-156, https://doi.org/10.1016/j.jsg.2020.104156.

Chester, F. M., and Chester, J. S., 1998, Ultracataclasite structure and friction processes of the Punchbowl fault, San Andreas system, California, Tectonophysics, v. 295, p. 199-221,

Chester, F.M., Evans J. P., and R. L Biegel, R. L,1993, Internal structure and weakening mechanisms of the San Andreas fault. Journal of Geophysical Research, v. 98, p. 771-786, 10.1016/S0040-1951(98)00121-8.

Chester, F. M., Logan, J. M.,1986, Implications for mechanical properties of brittle faults from observations of the Punchbowl fault zone, California. Pure and Applied Geophysics, v. 124, p. 79-106 **doi:10.1007/bf00875720.**

Crouch, K. A., 2022, Shallow Composition and Structure of the San Gabriel Fault, California in Drill Core and Geophysical Logs: Implications for Fault Slip and Energetics" All Graduate Theses and Dissertations. *https://digitalcommons.usu.edu/etd/8451*, DOI: https://doi.org/10.26076/a629-b091.

Crouch, K. A., and Evans, J. P., in revision, Composition and structure of the upper part of the San Gabriel fault; Implications for Fault Properties and Seismic Processes, to: Tektonika.

d' Alessio, M.A., Blythe, A.E., Bürgmann, R. , 2003, No frictional heat along the San Gabriel fault, California: Evidence from fission-track thermochronology. *Geology*, v. 31, p. 541–544. doi: https://doi.org/10.1130/0091-7613(2003)031<0541:NFHATS>2.0.CO;2.

De Bresser, J.H.P., and Spiers, C.J., 1997, Strength characteristics of the r, f, and c slip systems in calcite: Tectonophysics, v. 272, p. 1–23, doi:10.1016/S0040-1951(96)00273-9.

Dibblee, T. W., & Minch, J., 2002, Geologic map of the Valyermo quadrangle, Los Angeles County, California. Dibblee Geological Foundation. Retrieved from https://ngmdb.usgs.gov/Prodesc/proddesc_71715.htm

Dibblee, T.W. Jr., and Carter, B, 2002, Geologic Map of the Condor Peak Quadrangle, Los Angeles, CA, Dibblee Geological Foundation, Map DF-84, scale 1:24000.

Dolan, J. F., & Haravitch, B., 2014, How Well Do Surface Slip Measurements Track Slip at Depth in Large Strike-Slip Earthquakes? The Importance of Fault Structural Maturity in Controlling on-Fault Slip versus off-Fault Surface Deformation, Earth and Planetary Science Letters, v. 388, p. 38-47. doi: 10.1016/j.epsl.2013.11.043.

Duan, Q., Yang, X., Ma, S., Chen, J. and Chen, J., 2016, Fluid–rock interactions in seismic faults: Implications from the structures and mineralogical and geochemical compositions of drilling cores from the rupture of

the 2008 Wenchuan earthquake, China, Tectonophysics, v. 666, p.260-280, https://doi.org/10.1016/j.tecto.2015.11.008.

Edwards, N.P., Webb, S.M., Krest, C.M., van Campen, D., Manning, P.L., Wogelius, R.A., and Bergmann, U., 2018, A new synchrotron rapid-scanning X-ray fluorescence (SRS-XRF) imaging station at SSRL beamline 6-2, Journal of Synchrotron Radiation, v. 25, p. 1565-1573, doi: 10.1107/S1600577518010202.

Evans, J.P. and Chester, F.M., 1995, Fluid-rock interaction in faults of the San Andreas system: Inferences from San Gabriel fault rock geochemistry and microstructures, Journal of Geophysical Research: Solid Earth, v.100, p.13007-13020, DOI:10.1029/94JB02625.

Faulkner, D.R., Lewis, A.C., and Rutter, E.H., 2003, On the internal structure and mechanics of large strike-slip fault zones: Field observations of the Carboneras fault in southeastern Spain: Tectonophysics, v. 367, p. 235–251, doi:10.1016/S0040-1951(03)00134-3.

Faulkner, D. R., Jackson, C. A. L., Lunn, R. J., Schlische R.W., Shipton Z.K., Wibberley, C.A.J. Withjack, M.O., 2010, A review of recent developments concerning the structure, mechanics and fluid flow properties of fault zones, Journal of Structural Geology, v. 32, p. 1557-1575, https://doi.org/10.1016/j.jsg.2010.06.009.

Ferrill, D.A., Morris, A.P., Evans, M.A., Burkhard, M., Groshong, R.H., and Onasch, C.M., 2004, Calcite twin morphology: A low-temperature deformation geothermometer: Journal of Structural Geology, v. 26, p. 1521–1529, doi:10.1016/j.jsg.2003.11.028.

Fialko, Y., Sandwell, D., Simons, M. and Rosen, P., 2005, Three-dimensional deformation caused by the Bam, Iran, earthquake and the origin of shallow slip deficit, Nature, v. 435, p.295-299, doi: 10.1038/nature03425.

Field, E. H., Arrowsmith, R. J., and 17 others, 2014, Uniform California Earthquake Rupture Forecast, Version 3 (UCERF3)—The Time-Independent Model. *Bulletin of the Seismological Society of America* 2014; v. 104, p.1122–1180. doi: https://doi.org/10.1785/0120130164.

Forand, D., Evans, J. P., Janecke, S. U., & Jacobs, J., 2017, Insights into fault processes and the geometry of the San Andreas fault system: Analysis of core from the deep drill hole at Cajon Pass, California. Geological Society of America *Bulletin*. https://doi.org/10.1130/B31681.1.

Fusseis, F., Xiao, X., Schrank, C. and De Carlo, F., 2014, A brief guide to synchrotron radiation-based microtomography in (structural) geology and rock mechanics, Journal of Structural Geology, v. 65, p.1-16, https://doi.org/10.1016/j.jsg.2014.02.005.

Goguel, R., 1983, The rare alkalis in hydrothermal alteration at Wairakei and Broadlands, geothermal fields, N.Z., Geochimica et Cosmochimica Acta, v., 47, p. 429-437,

https://doi.org/10.1016/0016-7037(83)90265-X.

Gratier, J.-P. Richard, J., Renard, F., Mittempergher, S., Doan, M-L., Di Toro, G., Hadizadeh J., and Boullier, A-M., 2011, Aseismic sliding of active faults by pressure solution creep: Evidence from the San Andreas Fault Observatory at Depth, Geology, v. 39, p. 1131-1134, doi:10.1130/G32073.1.

Harris, R. A., and Day, S. M. 1997, Effects of a Low-Velocity Zone on a Dynamic Rupture, Bulletin of the Seismological Society of America, v. 87, pp. 1267-1280, https://doi.org/10.1785/BSSA0870051267.

Hauksson, E. and Meier, M.A., 2019, Applying depth distribution of seismicity to determine thermo-mechanical properties of the seismogenic crust in southern California: comparing lithotectonic blocks, Pure and Applied Geophysics, v.176, p.1061-1080, https://doi.org/10.1007/s00024-018-1981-z.

Hernandez, J.L., 2011, Preliminary Geologic Map of the Lake Hughes 7.5' Quadrangle, Los Angeles County, California. California Geologic Survey.

Holdsworth, R. E., Van Diggelen, E. W. E., Spiers, C. J., De Bresser, J. H. P., Walker, R. J., & Bowen, L, 2011, Fault rocks from the SAFOD core samples: Implications for weakening at shallow depths along the San Andreas Fault, California. Journal of Structural Geology, *33*, 132–144. https://doi.org/10.1016/j.jsg.2010.11.010.

Irwin, W. P., 1990, Geology and plate-tectonic development-San Andreas Fault, in The San Andreas Fault System, California, Wallace, R. E., ed., U. S. Geological Survey Professional Paper 1515, p. 61-82.

Isaacs A. J., J. P. Evans, P. T. Kolesar, T. Nohara 2008, Composition, microstructures, and petrophysics of the Mozumi fault, Japan: In situ analyses of fault zone properties and structure in sedimentary rocks from shallow crustal levels, J. Geophysical Research, v. 113, B12408, doi:10.1029/2007JB005314.

Jacobs, J. R., Evans, J. P, and Kolesar, P. T., 2006, Chemical alteration in fault zones as sinks for "missing" earthquake energy, in R. Abercrombie, H. Kanamori, and G. di Toro, eds., AGU Monograph 170, Earthquakes: Radiated Energy and the Physics of Faulting, p. 181-192.

Jefferies, S.P., Holdsworth, R.E., Wibberley, C.A.J., Shimamoto, T., Spiers, C.J., Niemeijer, A.R., and Lloyd, G.E., 2006, The nature and importance of phyllonite development in crustal-scale fault cores: An example from the Median Tectonic Line: Japan: Journal of Structural Geology, v. 28, p. 220–235, doi:10.1016/j.jsg.2005.10.008.

Jenne, E. A. 1968. Controls on Mn, Fe, Co, Ni, Cu, and Zn Concentrations in Soils and Water: the Significant Role of Hydrous Mn and Fe Oxides. Advances in Chemistry, p. 337–387.doi:10.1021/ba-1968-0073.ch021.

Jeppson, T. N., and Tobin, H. J. (2015), San Andreas fault zone velocity structure at SAFOD at the core, log, and seismic scales, Journal of Geophysical Research, v. 120, p. 4983– 4997, doi:10.1002/2015JB012043.

Jeppson, T. N., Bradbury, K. K., and Evans, J. P. (2010), Geophysical properties within the San Andreas Fault Zone at the San Andreas Fault Observatory at Depth and their relationships to rock properties and fault zone structure, Journal of Geophysical Research, v. 115, B12423, doi:10.1029/2010JB007563.

Kaduri, M., Gratier, J.P., Renard, F., Çakir, Z. and Lasserre, C., 2017, The implications of fault zone transformation on aseismic creep: Example of the North Anatolian Fault, Turkey, Journal of Geophysical Research: Solid Earth, v.122, p.4208-4236. https://doi.org/10.1002/2016JB013803.

Kaneko, Y. and Fialko, Y., 2011, Shallow slip deficit due to large strike-slip earthquakes in dynamic rupture simulations with elasto-plastic off-fault response, Geophysical Journal International, v. 186, p. 1389–1403, doi: 10.1111/j.1365-246X.2011.05117.x.

Kelly, S. D., D. Hesterberg, B. Ravel, 2008, Analysis of Soils and Minerals Using X-ray Absorption Spectroscopy, in: April L. Ulery, L. Richard Drees, eds., Methods of Soil Analysis Part 5—Mineralogical Methods, 5.5, Soil Science Society of America.

Lachenbruch A. H., 1986, Simple models for the estimation and measurement of frictional heating by an earthquake. U S Geological Survey Open File Report 86–508, 13p.

Los Angeles Department of Water and Power (LADWP), 2019, Final Report of San Andreas Coring Operation Near Elizabeth Lake Tunnel, California, https://doi.org/10.17605/OSF.IO/2VN6X.

Marchandon, M., Hollingsworth, J., and Radiguet, M., 2021, Origin of the shallow slip deficit on a strike-slip fault: Influence of elastic structure, topography, data coverage, and noise, Earth and Planetary Science Letters, v.554, 116696, https://doi.org/10.1016/j.epsl.2020.116696.

Marone, C. and Saffer, D. M., 2007, Fault Friction and the Upper Transition From Seismic to Aseismic Faulting, in The Seismogenic Zone of Subduction Thrust Faults, p. 346-369, Eds. Dixon, T. H. and Moore, J. C., 692 p., Columbia University Press.

Marone, C., and C. H. Scholz, 1988, The depth of seismic faulting and the upper transition from stable to unstable slip regimes, Geophysical Research Letters, v.15, p.621–624. doi:10.1029/GL015i006p00621.

Mitchell, T. M., & Faulkner, D. R. (2009). The nature and origin of off-fault damage surrounding strike-slip fault zones with a wide range of displacements: A field study from the Atacama fault system, northern Chile. Journal of Structural Geology, v.31, p. 802–816. https://doi.org/10.1016/j.jsg.2009.05.002.

Mitra, G., 1984, Brittle to ductile transition due to large strains along the White Rock thrust, Wind River Mountains, Wyoming: Journal of Structural Geology v. 6, p. 51-61, https://doi.org/10.1016/0191-8141(84)90083-X.

Moore, D. E., Rymer, M. J., 2012, Correlation of clayey gouge in a surface exposure of serpentinite in the San Andreas Fault with gouge from the San Andreas Fault Observatory at Depth (SAFOD), Journal of Structural Geology, v. 38, p. 51-60, https://doi.org/10.1016/j.jsg.2011.11.014.

Mulholland, W., 1918, Earthquakes in their relation to the Los Angeles Aqueduct: Bulletin Seismological Society of America, v. 8, p. 13-19.

Nevitt, J.M., Brooks, B.A., Catchings, R.D., Goldman, M.R., Ericksen, T.L. and Glennie, C.L., 2020, Mechanics of near-field deformation during co-and post-seismic shallow fault slip, Scientific Reports, v.10, p. 1-13, DOI: 10.1038/s41598-020-61400-9.

Niemeijer, A., Di Toro, G., Griffith, A.W., Bistacchi, A., Smith, S.A.F., and Nielsen, S., 2012, Inferring earthquake physics and chemistry using an integrated field and laboratory approach: Journal of Structural Geology, v. 39, p. 2–36, doi:10.1016/j.jsg.2012.02.018.

Nourse, J.A., 2002, Middle Miocene reconstruction of the central and eastern San Gabriel Mountains, southern California, with implications for evolution of the San Gabriel fault and Los Angeles basin, Geological Society of America Special Paper 365, p. 161–185.

Powell, R.E., 1993, Balanced palinspastic reconstruction of pre–late Cenozoic paleogeography, southern California, in Powell, R.E., et al., eds., The San Andreas fault system: Displacement, palinspastic reconstruction, and geologic evolution: Geological Society of America Memoir 178, p. 1–106.

Renard F., Cordonnier B., Dysthe D.K., Boller E., Tafforeau P., Rack A., 2016, A deformation rig for synchrotron microtomography studies of geomaterials under conditions down to 10-km depth in the Earth. Journal of Synchrotron Radiation, v. 23 (Pt 4):1030-4. doi:10.1107/S1600577516008730.

Rice, J. R., and Tse, S. T., 1986, Dynamic motion of a single degree of freedom system following a rate and state-dependent friction law, Journal of Geophysical Research, v. 91, p. 521–530, https://doi.org/10.1029/JB091iB01p00521.

Richard, J., Gratier, J.-P., Doan, M.-L.,.Boullier, A.-M, and Renard, F., 2014, Rock and mineral transformations in a fault zone leading to permanent creep: Interactions between brittle and viscous mechanisms in the San Andreas Fault, J. Geophys. Res. Solid Earth,119,8132–8153, doi:10.1002/2014JB011489.

Rollinson, H. and Pease, V., 2021, Using Geochemical Data: To Understand Geological Processes, Cambridge University Press.

Ross, D. C., 1984 Possible Correlations of basement rocks across the San Andreas, San Gregorio-Hosgri, and Rinconada-Reliz-King City Faults, California: U.S. Geological Survey Professional Paper 1317.

Roten, D., Olsen, K. B., and Day, S. M., 2017, Off-fault deformations and shallow slip deficit from dynamic rupture simulations with fault zone plasticity, Geophysical Research Letters, v. 44, https://doi.org/10.1002/2017GL074323.

Rowe, C.D., Griffith, W.A., 2015. Do faults preserve a record of seismic slip: a second opinion. Journal of Structural Geology, v. 78, p. 1–26, https://doi.org/10.1016/j.jsg.2015.06.006.

Rowe, C.D., Meneghini, F., Moore, J.C., 2011. Textural record of the seismic cycle: strain-rate variation in an ancient subduction thrust. Geological Society of London, Special Publication 359, p. 77–95. https://doi.org/10.1144/SP359.5.

Rumbiak, U., Lai C-K.,, Al Furqan, R., Rosana, M., Yuningsih, E., Tsikouras, B., Ifandi, E., Malik, A. I. A. b A., Chen, H., 2021. Geology, alteration geochemistry, and exploration geochemical mapping of the Ertsberg Cu-Au-Mo district in Papua, Indonesia, Journal of Geochemical Exploration, v. 232, https://doi.org/10.1016/j.gexplo.2021.106889.

Scharer, K., and Streig, A., 2019, The San Andreas Fault system: Complexities along a major transform fault system and relation to earthquake hazards, in Duarte, J.C., ed., Transform Plate Boundaries and Fracture Zone: Elsevier, p. 249–269, https://doi.org/10.1016/B978-0-12-812064-4.00010-4.

Scharer, K.M., and Yule, D., 2020, A maximum rupture model for the southern San Andreas and San Jacinto Faults, California, derived from paleoseismic earthquake ages: observations and limitations: Geophysical Research Letters, v. 47, doi:10.1029/2020GL088532.

Schleicher, A.M., Tourscher, S.N., van der Pluijm, B.A., and Warr, L.N., 2009, Constraints on mineralization, fluid-rock interaction, and mass transfer during faulting at 2–3 km depth from the SAFOD drill hole, Journal of Geophysical Research: Solid Earth, v. 114, B04202, doi:10.1029/2008JB006092

Scholz, C. H., 2019, The Mechanics of Earthquakes and Faulting, 3rd edition, Cambridge University Press, 493 p.

Schulz, S.E., Evans, J.P., 1998, Spatial variability in microscopic deformation and composition of the Punchbowl fault, Southern California: implications for mechanisms, fluid-rock interaction, and fault morphology. Tectonophysics v. 295, p. 223-244, https://doi.org/10.1016/S0040-1951(98)00122-X.

_____, 2000, Mesoscopic structure of the Punchbowl Fault, Southern California and the geologic and geophysical structure of active strike-slip faults. Journal of Structural Geology, v.22, p.913–930. https://doi.org/10.1016/s0191-8141(00)00019-5.

Scott, C., Champenois, J., Klinger, Y., Nissen, E., Maruyama, T., Chiba, T., and Arrowsmith, R., 2019, The 2016 M7 Kumamoto, Japan, earthquake slip field derived from a joint inversion of differential Lidar topography, optical correlation, and InSAR surface displacements: Geophysical Research Letters, v. 46, p. 6341–6351, doi:10.1029/2019GL082202.

Shipton, Z.K. Evans, J.P. Abercrombie, R.E. and Brodsky, E.E., 2006, The missing sinks: slip localization in jeffriiesToro, eds. Earthquakes: Radiated Energy and the Physics of Faulting, pp. 217-222. Washington, DC.: American Geophysical Union Monograph 170.

Sibson, R.H., 1986, Earthquakes and rock deformation in crustal fault zones, Annual Review of Earth and Planetary Sciences, v.14, p.149-175, DOI: 10.1146/annual.ea.14.050186.001053.

Simpson, C., 1985, Deformation of granitic rocks across the brittle-ductile transition, Journal of Structural Geology, v. 7, p. 503-511,https://doi.org/10.1016/0191-8141(85)90023-9.

Silver, L. T., and James, E. W., 1988, Geologic setting and lithologic column of the Cajon Pass Deep Drillhole, Geophysical Research Letters, v. 15, p. 941-944, https://doi.org/10.1029/GL015i009p00941.

Smith, S. A. F., Bistacchi, A., Mitchell, T. M., Mittempergher, S., Di Toro, G., 2013, The structure of an exhumed intraplate seismogenic fault in crystalline basement, *Tectonophysics*, v. 599, p. 29– 44. https://doi.org/10.1016/j.tecto.2013.03.031.

Sohn, R.A. and Menke, W., 2002, Application of maximum likelihood and bootstrap methods to nonlinear curve-fit problems in geochemistry, Geochemistry, Geophysics, Geosystems, v. 3, p.1-17, DOI: 10.1029/2001gc000253.

Spotila, J.A., House, M.A., Blythe, A.E., Niemi, N.A., and Bank, G.C., 2002, Controls on the erosion and geomorphic evolution of the San Bernardino and San Gabriel Mountains, southern California: Special Paper 365: Contributions to Crustal Evolution of the Southwestern United States, p. 205–230, doi:10.1130/0-8137-2365-5.205.

Studnicky, C., 2021, Constraining Deformation Mechanisms of Fault Damage Zones: A Case Study of the Shallow San Andreas Fault at Elizabeth Lake, Southern California. All Graduate Theses and Dissertations. 8134. https://digitalcommons.usu.edu/etd/8134.

Sturchio, N. C., Antonio, M. R., Soderholm, L., Sutton, S. R., and Brannon, J. C., 1998, Tetravalent uranium in calcite, Science, v. 281, p. 971-973.

Sutherland, M., Keaton, J.R., Heron, C., 2013, Correlating surface geology with 1913-vintage as-built geology across the San Andreas fault for seismic enhancement of the Elizabeth Tunnel, Los Angeles Aqueduct, Geological Society of America Abstracts with Programs. v. 45, No. 6, p.23.

Tayyebi, A., Telling, J., Hudnut, K., Davis, C. Glennie, C., 2017, 100 Years of accumulated deformation at depth observed in the Elizabeth Lake Tunnel, southern San Andreas Fault: Abstract G43C-04, American Geophysical Union Fall Meeting Abstracts.

Timofeev, A., Migdisov, A. A, A. E. Williams-Jones, A. E., Roback, R., Nelson, A. T., and Xu, H. W., 2018, Uranium Transport in Acidic Brines under Reducing Conditions. Nature Communications 9 http://dx.doi.org/10.1038/s41467-018-03564-7.

Townend, J. et al., 2017, Petrophysical, geochemical, and hydrological evidence for extensive fracture-mediated fluid and heat transport in the Alpine Fault's hanging-wall damage zone. Geochemistry, Geophysics, Geosystems, v. 18, p. 4709–4732. https://doi.org/10.1002/2017GC007202

Turcotte, D. L., Tag, P. H., and Cooper, R. F., 1980, A steady-state model for the distribution of stress and temperature on the San Andreas Fault, Journal of Geophysical Research, v. 85, p. 6224-6230.

Utada, M., 2001, Zeolites in burial diagenesis and low-grade metamorphic rocks: Reviews in Mineralogy and Geochemistry, v. 45, p. 276–304, doi:10.2138/rmg.2001.45.9.

Webb, S. M., 2011, The MicroAnalysis Toolkit: X-ray Fluorescence Image Processing Software, Amer. Insti Phys. Conf. Proc.1365, 196-199. DOI: 10.1063/1.3625338. https://doi.org/10.1063/1.3625338.

Webb, S. M., 2020, *SIXPACK*: a graphical user interface for XAS analysis, in, X-Ray Absorption Spectroscopy and Related Techniques, International Tables for Crystallography, C. T. Chantler, F. Boscherini and B. Bunker, eds., https://doi.org/10.1107/S1574870720003456,

Wechsler, N., Allen, E.E., Rockwell, T.K., Girty, G., Chester, J.S., and Ben-Zion, Y., 2011, Characterization of pulverized granitoids in a shallow core along the San Andreas Fault, Littlerock, CA: Geophysical Journal International, v. 186, p. 401–417, doi:10.1111/j.1365-246X.2011.05059.x.

Weisenberger, T., and Bucher, K., 2010, Zeolites in fissures of granites and gneisses of the Central Alps: Journal of Metamorphic Geology, v. 28, p. 825–847, doi:10.1111/j.1525-1314.2010.00895.x.

Wibberley, C.A.J. and Shimamoto, T., 2003, Internal structure and permeability of major strike-slip fault zones: the Median Tectonic Line in Mie Prefecture, Southwest Japan, Journal of Structural Geology v.25, p.59-78, https://doi.org/10.1016/S0191-8141(02)00014-7.

Wibberley, C.A.J., Yielding, G., and Di Toro, G., 2008, Recent advances in the understanding of fault zone internal structure; a review. In: Wibberley, C.A.J., Kurz, W., Imber, J., Holdsworth, R.E., Collettini, C. (Eds.), Structure of Fault Zones: Implications for Mechanical and Fluid-flow Properties, Geological Society of London Special Publication, v. 299, p. 5-33.

Williams, R. T., Rowe, C. D., Okamoto, K., Savage, H. M., & Eves, E. 2021, How fault rocks form and evolve in the shallow San Andreas fault. Geochemistry, Geophysics, Geosyste*ms*, v. 22, e2021GC010092. https://doi.org/10.1029/2021GC010092.

Woodcock, N., and Mort, K., 2008, Classification of fault breccias and related fault rocks, Geological Magazine, v. 145, p. 435-550, https://doi.org/10.1017/S0016756808004883.

Xu, X., Tong, X., Sandwell, D. T., Milliner, C. W.D., Dolan, J. F., Hollingsworth, J., Leprince, S., and Ayoub, F., 2016, Refining the shallow slip deficit, Geophysics Journal International, v. 204, 1867–1886, doi:10.1093/gji/ggv563.

Zielke, O., Arrowsmith, J.R., Ludwig, L.G., and Akciz, S.O., 2010, Slip in the 1857 and Earlier Large Earthquakes Along the Carrizo Plain, San Andreas Fault: Science, v. 327, p. 1119–1122, doi:10.1126/science.1182781.

Appendix. Synchrotron methods and conditions

We examined the elemental distribution of rocks in this section on three beamlines at the Stanford Synchrotron Radiation Laboratory (SSRL). The SPEAR (Stanford Positron Electron Accelerating Ring) storage ring operates at 500 mA beam current at 3.0 GeV, topped off every 5 minutes. For the thin-section samples, we collected data for XRF-maps on elements from sulfur to arsenic on beamlines 2-3, 6-2, and 10-2. Details of analysis conditions are provided below. The energies and spatial resolution for all samples measured across the three different beamlines are provided in the table below.

The SSRL beamline 2-3 enables the highest resolution mapping. On beamline 2-3 we use a Si (111) double crystal monochromator for incident X-ray energy selection. The fluorescent lines of the elements are measured in an open-air hutch using a single-channel silicon drift Hitachi Vortex detector coupled to a Quantum Detectors Xspress3 multi-channel analyzer. Standard 2.7 x 4.6 cm thin polished thin sections are mounted on a rotating base at 45° to the incident X-ray beam and 2 or 5 mm regions were rastered in the microbeam while data were collected continuously during stage motion.

We examined 5 x 7.5 cm thin sections for large-scale XRF imaging on beamline 10-2, now 7-2. Thin sections were mounted on a large flat plate and raster scanned at 45° relative to the incident X-ray beam. We use the SRS-XRF method with a Si (111) double crystal monochromator to select the incident energy. The fluorescent X-rays are measured with a four-element Hitachi Vortex ME4 silicon drift detector coupled to a Quantum Detectors Xspress3 multi-channel analyzer system for elemental XRF mapping in an open hutch.

On beamline 6-2 (see Edwards et al., 2018) we examined an ~80 cm long portion of drill core from the San Andreas Fault (Figure 4). Beamline 6-2 uses a continuous rapid-scan system with a sample area of up to 1000×600 mm, with 25–100 μm resolution provided by pinhole apertures. The fluorescence X-rays are measured with a four-element Hitachi Vortex ME4 silicon drift detector coupled to a Quantum Detectors Xspress3 multi-channel analyzer system for elemental XRF mapping.

The conditions used for the samples examined are summarized below.

Sample number	beamline	spot size (μm)	dwell time (ms)	Energy (eV)	Point range and total time (sec)
SGF 51-1	10-2	25	25	8000	569 x 134; 4837
SGF 71-1	10-2	25	25	12500	793 x 684; 16202
SGF 71-1	10-2	25	25	12500	739 x 538; 11328
SGF 65A	10-2	10, 25, 50,75	25	12500	1501 x 367; 14937
SGF 65A	2-3	2, 5	25	7200	281x 601; 5367
SGF 96.1	10-2	25	25	12500	946 x 234; 6154
SGF 96.1	10-2	5	25	12500	1017 x 456; 12808
SGF 96-1	2-3	1.5	25	7200	1152 x 211; 7702
LE 4-130	2-3	2	25	7200	17092s
LE 6-134	10-2	25	25	13000	4336
LE 6-134	2-3	4, 5	25	7200	1865
LE 2-355	2-3	15	25	7200	846x139, 3567
LE 6-433	10-2	50	15	13000	1709 x 613; 18848
LE 6-433	2-3	15	10	7500	646 x 25725 4184
SAF LE core	6-2	25,50	10	11000	7754,10047;8541,12041
SAF core E	6-2	50	20	11000	12022

Table 1. Whole-rock major, minor, and trace element geochemical data for the San Andreas Fault zone from the Lake Elizabeth drill core site.

Table 2. Whole-rock data major, minor, and trace element geochemical data for the San Gabriel Fault from the CHSRA drill site.

Supplemental Files

Supplemental File 1. Enrichment ratios for San Andreas Fault samples.

Supplemental File 2. Calculated values of elemental enrichment or depletion of damaged zone samples, of San Gabriel Fault samples.

Supplemental File 3. Calculated values of elemental enrichment or depletion of fault gouge samples, of San Gabriel Fault samples.

Supplemental Figure 1. XRF maps of a zoomed-in portion of the whole core San Andreas core. The analysis examines the elemental distribution of a part of a damage zone near Fe-rich fault gouge A) Visible light image of the core showing the location of the image. Fractured and altered rocks encompass a thin slip surface (ss), cataclasite (cata), and Fe-rich gouge (g). Rocks to the left of the slip zone are barely cohesive gouge/pulverized rock, and the damage zone rocks to the right are moderately indurated. B) Elemental maps of Fe, Mn, Cr, and Ti show they are enriched in a sheared zone on the left side of the image, and in zones with sharp boundaries that cut into the highly damaged rocks. C) Elemental maps of Ca and K, and tricolor maps of Fe-Ca-Ti, and Mn-Ca-K. The metals are enriched in zones that surround K- and Ca-rich regions that appear to be zones of earlier-formed cataclasite, with sharp, straight boundaries. Thin zones have concentrations of Cr and Ti (Cr-Ti). In places iron and manganese fills fractures in the earlier cataclasite fragment (Fe).

Supplemental Figure 2. Cross-plots among the transition elements for the San Andreas core sample analyses. A. Mn-Fe, Ni-Cr, and Cr-Mn for part of the the SAF large core sample shown in Supplemental Figure 1. D and E Correlation plots for sample – 4-130. For Fm-Fe and Cr-Mn.

Supplemental Figure 3. Cross-plots among the transition elements for the SAF thin-section sample analyses for sample LE 2-355. A. Mn-Fe B. Ni-Mn, C. Ti-Mn, and D. Cr-Mn.

Supplemental Figure 4. Elemental maps and correlation plots for sample 6-433. A. Fe-Ca-K and Fe-Ca-Mn high-magnification tricolor maps of highly sheared Fe-rich zones that cut protolith grains that have Ca (probably showing the presence of calcite). B. Cross-plot of iron and manganese in the mapped area. C. Correlation plots of Cr-Fe, Cr-Mn, Ti-Cr, Ni-Cr, and Ni-Mn in the mapped area of figure A..